NASA Contractor Report 158972

SIGNIFICANCE OF READIATION MODELS IN INVESTIGATING
THE FLOW PHENOMENA AROUND A JOVIAN ENTRY BODY

S. N. Tiwari and S. V. Subramanian

OLD DOMINION UNIVERSITY RESEARCH FOUNDATION
Norfolk, VA 23508

NASA
National Aeronautics and
Space Administration

Langley Research Center
Hampton, Virginia 23665

DEPARTMENT OF MECHANICAL ENGINEERING AND MECHANICS
SCHOOL OF ENGINEERING
OLD DOMINION UNIVERSITY
NORFOLK, VIRGINIA

SIGNIFICANCE OF RADIATION MODELS IN

INVESTIGATING THE FLOW PHENOMENA AROUND

A JOVIAN ENTRY BODY

By

S. N. Tiwari

and

S. V. Subramanian

FOREWORD

This is a final report of the work completed on the research project "Nongray Radiative Gas Flows Coupled with Ablation Around a Jovian Entry Body." The work was supported by the NASA/Langley Research Center through research contract/task authorization NAS1-14193-26. The contract was monitored by Dr. Randolph A. Graves, Jr. of SSD-Aerothermodynamics Branch.

TABLE OF CONTENTS

LIST OF FIGURES

(Cont'd)

SIGNIFICANCE OF RADIATION MODELS IN INVESTIGATING
THE FLOW PHENOMENA AROUND A JOVIAN ENTRY BODY

By

S. N. Tiwari[1] and S. V. Subramanian[2]

SUMMARY

Formulation is presented to demonstrate the significance of a sim-
plified radiation model in investigating the flow phenomena in the viscous
radiating shock layer of a Jovian entry body. The body configurations
used in this study are a 55° sphere cone and a 50° hyperboloid. A nongray
absorption model for hydrogen-helium gas is developed which consists of
30 steps over the spectral range of 0 to 20 eV. By employing this model,
results were obtained for temperature, pressure, density, and radiative
flux in the shock layer and along the body surface. These are compared with
results of two sophisticated radiative transport models available in the
literature. Use of the present radiation model results in significant
reduction of computational time. Results of this model are found to be in
general agreement with results of other models. It is concluded that use
of the present model is justified in investigating the flow phenomena around
a Jovian entry body because it is relatively simple, computationally fast,
and yields fairly accurate results.

INTRODUCTION

The problem of radiative heating of planetary entry bodies has been
investigated extensively in the literature (refs. 1 to 3). At Jovian
entry conditions, radiative heating constitutes the major portion of heat
transferred to the entry body. In order to assess the magnitude of radiative
heating of the Jovian entry body, it is essential to employ meaningful

[1] Professor, Department of Mechanical Engineering and Mechanics, Old Dominion
University, Norfolk, Virginia 23508.

[2] Graduate Research Assistant, Old Dominion University Research Foundation,
Norfolk, Virginia 23508.

radiative transport models in analyzing the shock-layer flow phenomena. This, in turn, requires realistic models for absorption by the hydrogen-helium gas and other species (such as ablative products) that may be present in the shock layer. By employing detailed information on the line and continuum absorption, Nicolet (refs. 4 to 6) has developed a fairly sophisticated radiative transport model for application to planetary entry conditions. Use of such models requires a considerably long computational time while analyzing the shock-layer flow phenomena. In fact more than 75 percent of the computational time is spent in the radiative transport part of the radiating hypersonic flow solutions. It is, therefore, desirable to develop simplified radiative transport models which could be used to provide a quick parametric study of the complicated problem involving nonequilibrium chemistry and ablative products.

For absorption by the hydrogen-helium gas, Sutton (ref. 7) has developed a 58-step gray gas model, the results of which compare well with Nicolet's detailed model. For high-temperature Jovian entry conditions, it is possible to further reduce the number of steps in the spectral range of interest and provide a fairly simplified absorption model. Thus, the purpose of this study is to develop a computationally fast, relatively simple, and reasonably accurate model for spectral absorption by the hydrogen-helium gas. The feasibility of this model is established by comparing the results obtained by this model with the results of Sutton's 58-step model and Nicolet's detailed model.

NOMENCLATURE

C_i mass fraction of species i in the shock layer, ρ_i/ρ

C_p equilibrium specific heat of mixture, $\Sigma\ C_i\ C_{p,i}$

$C_{p,i}$ specific heat of species i, $C_{p,i}^*/C_{p,\infty}^*$

D_{ij} binary diffusion coefficient

h specific enthalpy, h^*/V_∞^{*2} (also Planck constant)

H_T total enthalpy, $h = (u^2+v^2)/2$

J_i mass diffusion flux of species i,

$J_i^* R_N / \mu_{ref}^*$

k   thermal conductivity of mixture, $k^*/\mu_{ref}^* C_{p,\infty}^*$ (also Boltzmann constant)

Le   Lewis number, $\rho^* D_{ij}^* C_p^* / k^*$

M^* molecular weight of mixture

n   coordinate normal to the body surface n^*/R_N^*

p   pressure, $p^* / (\rho_\infty^* V_\infty^{*2})$

Pr   Prandtl number, $\mu^* C_p^* / k^*$

q_R net radiant heat flux, $q_R^{*'}/(\rho_\infty^* V_\infty^{*3})$

r   radius measured from axis of symmetry to a point on the body

surface, f^*/R_N^*

R^* universal gas constant

R_b^* radius of the body

R_N^* body nose radius (same as R_n^*)

s   coordinate along the body surface, s^*/R_N^*

T   temperature, T^*/T_{ref}^*

T_o^* reference temperature, 27315 °K

T_{ref}^* reference temperature, $V_\infty^* / C_{p,\infty}^*$

u   velocity tangent to body surface, u^*/V_∞^*

v   velocity normal to body surface, u^*/V_∞^*

α shock angle defined in figure 1

ϵ Reynolds number parameter or surface emittance

Θ body angle defined in figure 1

κ body curvature, $\kappa^* R_N^*$

κ_ν spectral absorption coefficient

μ viscosity of mixture, μ^*/μ_{ref}^*

μ_{ref}^* reference viscosity, $\mu^*(T_{ref}^*)$

ρ density of mixture, ρ^*/ρ^*_∞

σ^* Stefan Boltzmann constant

τ optical coordinate

τ_o optical thickness

Subscript

i   ith species

s   shock value

w   wall value

∞ free-stream condition

ν radiation frequency

BASIC FORMULATION

The physical model and coordinate system for a Jovian entry body are shown in figure 1. In this figure, s is the distance measured along the body surface and n is the distance normal to the body surface. The flow in the shock layer is considered to be that of an axisymmetric, viscous, radiating flow, local thermodynamic and chemical equilibrium. Furthermore, it is assumed that the radiative transport occurs within a one-dimensional, infinite planar slab (tangent slab approximation). Both inviscid as well as viscous shock-layer analyses are presented. The same radiation models are used in both analyses. In this section basic governing equations and boundary conditions for inviscid and viscous shock-layer flows are presented in most general form. These equations are usually transformed to alternate forms for computational convenience.

Inviscid Flow Equations

For the physical model considered, the governing equations for inviscid flow are expressed (refs. 8,9) as

Continuity.

$$(1/\Gamma)\ (\partial/\partial s)\ (\rho u) + (\rho u/r)\sin\ \Theta + (\partial/\partial n)\ (\rho v)$$

$$+ \rho v\ [(\kappa/\Gamma) + \cos\ \Theta/r] = 0 \tag{1}$$

4

s-momentum.

$$(u/\Gamma) \; (\partial u/\partial s) + v \; (\partial u/\partial n) + uv\kappa/\Gamma + (1/\rho\Gamma) \; (\partial p/\partial s) = 0 \tag{2}$$

n-momentum.

$$(u/\Gamma) \; (\partial v/\partial s) + v \; (\partial v/\partial n) - u^2\kappa/\Gamma + \rho^{-1} \; (\partial p/\partial y) = 0 \tag{3}$$

Energy

$$(u/\Gamma) \; (\partial h/\partial s) + v \; (\partial h/\partial n) - (u/\rho\Gamma) \; (\partial p/\partial s) - (v/\rho) \; (\partial p/\partial n)$$

$$+ \; (1/\rho) \; (\mathrm{div} \; q_R) = 0 \tag{4}$$

where

$$\Gamma = 1 + n\kappa$$

$$\mathrm{div} \; q_R = (\partial q_R/\partial n) + q_R \; (\kappa/\Gamma + \cos \theta/r)$$

It should be noted that the above equations are written in nondimensional form. Quantities to nondimensionalize these equations are defined in the nomenclature.

The equation of state for the gas, in general, can be expressed as

$$p = \rho \; T(R^*/M^* \; C_{p,\infty}) \tag{5}$$

where $C_{p,\infty}$ represents the specific heat of the gas at the free-stream conditions.

In order to solve the above set of governing equations, it is essential to specify appropriate boundary conditions at the body surface and the shock. The boundary conditions at the shock are calculated by using the Rankin-Hugoniot relations. At the wall, no-slip and no-temperature-jump boundary conditions are used. Consequently,

$$u(0,n) = u_w = 0 \quad , \quad v(0,n) = v_w = 0 \tag{6}$$

$$T(0,n) = T_w = \text{constant (specified)} \tag{7}$$

5

Viscous Flow Equations

Basic governing equations for viscous shock layer are obtained from the steady-state Navier-Stokes equations by keeping terms up to second order in the inverse square root of the Reynolds number, ϵ, as (refs. 9 to 11):

Continuity.

$$(\partial/\partial s)\ [(r+n\cos\theta)\rho u] + (\partial/\partial n)\ (\Gamma\zeta\rho v) = 0 \tag{8}$$

s-momentum.

$$\rho[(u/\Gamma)\ (\partial u/\partial s) + v(\partial u/\partial n) + uv\kappa/\Gamma] + \Gamma^{-1}(\partial p/\partial s)$$

$$= \epsilon^2[(\partial/\partial n)\ (\partial\psi) + \mu(2\kappa/\Gamma + \cos\theta/\zeta)\psi] \tag{9}$$

n-momentum.

$$\rho[(u/\Gamma)\ (\partial v/\partial s) + v\ (\partial v/\partial n) - u^2\kappa/\Gamma] + \partial p/\partial n = 0 \tag{10}$$

Energy.

$$\rho C_p[(u/\Gamma)\ (\partial T/\partial s) + v(\partial T/\partial n)] - [(u/\Gamma)\ (\partial p/\partial s) + v\ (\partial p/\partial n)]$$

$$= \epsilon^2\{(\partial/\partial n)\ [k(\partial T/\partial n)] + [(\kappa/\Gamma) + \cos\theta/\zeta]k(\partial T/\partial n)$$

$$- \sum_{i=1}^{N} J_i C_{p,i}(\partial T/\partial n) + \mu\psi^2\} - \text{div } q_R \tag{11}$$

Species continuity.

$$\rho[(u/\Gamma)\ (\partial C_i/\partial s) + v\ (\partial C_i/\partial n)] = (\epsilon^2/\Gamma\zeta)\ [(\partial/\partial n)\ (\Gamma\zeta J_i)] \tag{12}$$

where

$$\zeta = r + n\cos\theta \tag{13a}$$

$$\epsilon = \mu^*_{ref}/(\rho^*_\infty\ V^*_\infty\ R^*_N)^{1/2} \tag{13b}$$

$$\psi = \partial u/\partial n - u\kappa/\Gamma \tag{13c}$$

$$J_i = (\mu/Pr)\ L_e\ (\partial C_i/\partial n) \tag{13d}$$

The above equations are also written in nondimensional form, and quantities to nondimensionalize these equations are dfined in the nomenclature.

The expressions for the equation of state for a hydrogen-helium mixture are given by (refs. 12,13):

$$T^* = C_T[(p^*/1013250)^\ell/(\rho^*/0.001292)^k] \tag{14a}$$

$$H^* = C_H[(p^*/1013250)^m/(\rho^*/0.001292)^n]\ (R^*T_0^*/M^*) \tag{14b}$$

where quantities C_T, C_H, k, ℓ, m, and n are defined in the cited references.

Once again, the boundary conditions at the shock are calculated by using the Rankine-Hugoniot relations, and conditions at the body surface are given by equations (6) and (7).

RADIATION MODELS

An appropriate expression for the radiative flux q_R is needed for the solution of the energy equation presented in the previous section. This requires a suitable radiative transport model and a meaningful spectral model for variation of the absorption coefficient of the gas. In this section, appropriate expressions for the spectral and total radiative flux are given, and a detailed discussion on models for the spectral absorption by the hydrogen-helium gas is presented.

Radiative Flux Equations

The equations for radiative transport, in general, are integral equations which involve integration over both frequency spectrum and physical coordinates. In many physically realistic problems, the complexity of the three-dimensional radiative transfer can be reduced by introduction of the "tangent slab approximation." This approximation treats the gas layer as a one-dimensional slab in calculation of the radiative transport. Radiation in directions other than normal to either the body or shock is neglected in comparison. Discussions on the validity of this approximation for planetary entry conditions are given in references 14 to 18. The tangent slab approximation is employed in this study. It should be pointed out here that this approximation is used only for the radiative transport and not for the other flow variables.

For the present study, the equations of radiative transport are obtained for a gas confined between two infinite, parallel boundaries, the shock wave, and the body. This is shown in figure 2. For one-dimensional radiation, the equations of transfer for a nonscattering medium in local thermodynamic equilibrium are given by (refs. 19,20):

$$\mu(dI_\nu^+/d\tau_\nu) = B_\nu(\tau_\nu) - I_\nu^+ \tag{15a}$$

$$\mu(dI_\nu^-/d\tau_\nu) = B_\nu(\tau_\nu) - I_\nu^- \tag{15b}$$

where

$$\mu = \cos\theta \tag{16a}$$

$$\tau_\nu = \int_0^n \kappa_\nu(n)\ dn \tag{16b}$$

$$\tau_{0\nu} = \int_0^{n_s} \kappa_\nu(n)\ dn \tag{16c}$$

In the above equation, κ_ν and B_ν represent the frequency-dependent linear absorption coefficient and Planck function, respectively. Furthermore, it should be noted that I_ν^+ and I_ν^- correspond to positive and negative values of μ respectively. The boundary conditions for equations (15a) and (15b) can be expressed as

$$I_\nu^+(\tau_\nu,\mu) = I_\nu^+(0,\mu),\ \tau_\nu = 0 \tag{17a}$$

$$I_\nu^-(\tau_\nu,\mu) = I_\nu^-(\tau_{0\nu},\mu),\ \tau_\nu = \tau_{0\nu} \tag{17b}$$

By employing the above conditions, integration of equations (15a) and (15b) results in

$$I_\nu^+(\tau_\nu,\mu) = I_\nu^+(0,\mu)\ \exp(-\tau_\nu/\mu) + \int_0^{\tau_\nu} B_\nu(t)\ \exp[-(\tau_\nu - t)/\mu]\mu^{-1}\ dt \tag{18a}$$

$$I_\nu^-(\tau_\nu,\mu) = I_\nu^-(\tau_{0\nu},\mu)\ \exp[-(\tau_{0\nu} - \tau_\nu)/\mu]$$

$$-\int_{\tau_\nu}^{\tau_{0\nu}} B_\nu(t)\ \exp[-(\tau_\nu - t)/\mu]\mu^{-1}\ dt \tag{18b}$$

8

Equations (19a) and (18b) describe the radiation field in terms of the temperature field within the medium. The temperature field is expressed by the Planck function. The term $I_\nu^+(0,\mu) \exp(-\tau_\nu/\mu)$ in equation (18a) represents the radiant energy that originated at the body surface which has been attenuated by the factor $\exp(-\tau_\nu/\mu)$ as a result of absorption. The integral term represents the augmentation of I_ν^+ due to gaseous emission. A similar interpretation goes for equation (18b), with respect to shock surface.

Referring to figure 2, the spectral radiative flux is expressed in terms of intensity of radiation as (ref. 20):

$$q_{R\nu}(\tau_\nu) = \int_{4\Pi} I_\nu \cos\Theta \, d\Omega = 2\Pi \int_{-1}^{1} I_\nu(\tau_\nu,\mu) \, \mu \, d\mu \tag{19}$$

By noting that I_ν^+ and I_ν^- correspond to positive and negative values of μ, equation (19) can be expressed as

$$q_{R\nu}(\tau_\nu) = 2\Pi \int_0^1 I_\nu^+ \, \mu \, d\mu - 2\Pi \int_0^{-1} I_\nu^- \, \mu \, d\mu \tag{20}$$

The substitution of values for I_ν^+ and I_ν^- from equations (18a) and (18b) into equation (20) results in the one-dimensional expression for spectral radiative flux as (refs. 19,20):

$$q_{R\nu}(\tau_\nu) = 2\Pi \left\{ \int_0^1 I_\nu^+(0,\mu)e^{-\tau_\nu/\mu} + \int_0^{\tau_\nu} B_\nu(t) \, E_2(\tau_\nu - t) \, dt \right.$$

$$-\left[\int_0^1 I_\nu^-(\tau_{o\nu},-\mu)e^{-(\tau_{o\nu} - \tau_\nu)/\mu} \, \mu \, d\mu \right.$$

$$\left. \left. + \int_{\tau_\nu}^{\tau_{o\nu}} B_\nu(t) \, E_2(t - \tau_\nu) \, dt \right] \right\} \tag{21}$$

where $E_n(t)$ is the exponential integral function defined by

$$E_n(t) = \int_0^1 \mu^{n-2} e^{-t/\mu} \, d\mu \tag{22}$$

The expression for the net radiative flux at any location is given by

$$q_R(n) = \int_0^\infty q_{R\nu}(\tau_\nu) \, d\nu \tag{23}$$

Often, it is desirable to obtain separate relations for total radiative flux going towards the body and the bow shock. Upon denoting the radiative flux towards the shock by q_R^+ and towards the body by q_R^-, equation (23) can be written as

$$q_R(n) = q_R^+(n) - q_R^-(n)$$

$$= \int_0^\infty q_{R\nu}^+(\tau_\nu) \, d\nu - \int_0^\infty q_{R\nu}^-(\tau_\nu) \, d\nu \tag{24}$$

where

$$q_{R\nu}^+ = 2\pi \int_0^\infty \left[\int_0^1 I_\nu^+(0,\mu) e^{-\tau_\nu/\mu} \mu \, d\mu + \int_0^{\tau_\nu} B_\nu(t) \, E_2(\tau_\nu - t) \, dt \right] d\nu \tag{25a}$$

$$q_{R\nu}^- = 2\pi \int_0^\infty \left[\int_0^1 I_\nu^-(\tau_{o\nu},-\mu) e^{-(\tau_{o\nu} - \tau_\nu)/\mu} \mu \, d\mu \right.$$

$$\left. + \int_{\tau_\nu}^{\tau_{o\nu}} B_\nu(t) \, E_2(t - \tau_\nu) \, dt \right] d\nu \tag{25b}$$

for diffuse surfaces, $I_\nu^+(0,\mu)$ and $I_\nu^-(\tau_{o\nu},\mu)$ are independent of direction (i.e., independent of μ) and may be expressed in terms of surface radiosities $B_{1\nu}$ and $B_{2\nu}$ as

$$\pi I_\nu^+(0,\mu) = B_{1\nu} , \quad \pi \, I_\nu^-(\tau_{o\nu},\mu) = B_{2\nu} \tag{26}$$

Hence, equations (25a) and (25b) are expressed as

$$q_\nu^+(n) = 2 \int_0^\infty \left[B_{1\nu} \, E_3(\tau_\nu) + \pi \int_0^{\tau_\nu} B_\nu(t) \, E_2(\tau_\nu - t) \, dt \right] d\nu \tag{27a}$$

10

$$q_R^-(n) = 2 \int_0^\infty \left[B_{2\nu} E_3(\tau_{0\nu} - \tau_\nu) + \Pi \int_0^{\tau_\nu} B_\nu(t) E_2(\tau_\nu - t) dt \right] d\nu \qquad (27b)$$

The expressions for surface radiosities appearing in this equation are given by (ref. 20):

$$B_{1\nu} = \varepsilon_{1\nu} \left[\Pi B_\nu(T_w) \right] + 2 \rho_{1\nu} \left[B_{2\nu} E_3(\tau_{0\nu}) + \int_0^{\tau_{0\nu}} \Pi B_\nu(t) E_2(t) dt \right] \qquad (28a)$$

$$B_{2\nu} = \varepsilon_{2\nu} \left[\Pi B_\nu(T_s) \right] + 2 \rho_{2\nu} \left[B_{1\nu} E_3(\tau_{0\nu}) + \int_0^{\tau_{0\nu}} \Pi B_\nu(t) \right.$$

$$\left. \cdot E_2(\tau_{0\nu} - t) dt \right] \qquad (28b)$$

where $\rho_{1\nu}$ and $\rho_{2\nu}$ represent the surface reflectance of the body and the shock respectively. For nonreflecting surfaces, $\rho_{1\nu} = \rho_{2\nu} = 0$, and equations (28a) and (28b) reduce to

$$B_{1\nu} = \Pi \varepsilon_{1\nu} B_\nu(T_w), \quad B_{2\nu} = \Pi \varepsilon_{2\nu} B_\nu(T_s) \qquad (29)$$

Sometimes, it is convenient to express the radiative flux equations in terms of gas emissivities, defined by

$$\varepsilon_\nu^+ = 1 - 2E_3(\tau_\nu - t), \quad \varepsilon_\nu^- = 1 - 2E_3(t - \tau_\nu) \qquad (30)$$

By noting that

$$d\varepsilon_\nu^+ = -2E_2(\tau_\nu - t) dt, \quad d\varepsilon_\nu^- = 2E_2(t - \tau_\nu) dt$$

$$\varepsilon_\nu^+(t = 0) = 1 - 2E_3(\tau_\nu) = \varepsilon_b^+ = \varepsilon_w^+$$

$$\varepsilon_\nu^+(t = \tau_\nu) = 1 - 2E_3(0) = 1 - 2\left(\frac{1}{2}\right) = 0 = \varepsilon_\nu^-(t = \tau_\nu)$$

$$\varepsilon_\nu^-(t = \tau_{0\nu}) = 1 - 2E_3(\tau_{0\nu} - \tau_\nu) = \varepsilon_b^- = \varepsilon_s^-$$

equations (27a) and (27b) can be written as

11

$$q_R^+(n) = \int_0^\infty \left[2B_{1\nu} E_3(\tau_\nu) + \Pi \int_0^{\epsilon_w^+} B_\nu(\epsilon_\nu^+) \, d\epsilon_\nu^+ \right] d\nu \qquad (31a)$$

$$q_R^-(n) = \int_0^\infty \left[2B_{2\nu} E_3(\tau_{o\nu} - \tau_\nu) + \Pi \int_0^{\epsilon_s^-} B_\nu(\epsilon_\nu^-) \, d\epsilon_\nu^- \right] d\nu \qquad (31b)$$

If the radiative flux into the slab at the boundaries is neglected, then the first term on the right of equations (31a) and (31b) vanishes and the net radiative flux is given by

$$q_R(n) = \Pi \int_0^\infty \left[\int_0^{\epsilon_w^+} B_\nu(\epsilon_\nu^+) \, d\epsilon_\nu^+ - \int_0^{\epsilon_s^-} B_\nu(\epsilon_\nu^-) \, d\epsilon_\nu^- \right] d\nu \qquad (32)$$

Depending upon the particular assumptions made in a physical problem, use is made of either equations (27a) and (27b), (31a) and (31b), or equation (32) in obtaining the net radiative heat flux.

For mathematical convenience, exponential integrals often are approximated by appropriate exponential functions. There are a few standard procedures for doing this, and these are discussed in references 19 and 20. It has been demonstrated (see ref. 20, for example) that when the exponential integral of third order is approximated by

$$2E_3(z) = \exp(-2z) \qquad (33)$$

the radiative transport solutions are exact in the optically thin limit, and of satisfactory accuracy in the optically thick limit. By using equation (33), approximate expressions for the gas emissivities are obtained from equation (30) as

$$\epsilon_\nu^+ = 1 - \exp[2(t - \tau_\nu)] \qquad (34a)$$

$$\epsilon_\nu^- = 1 - \exp[2(\tau_\nu - t)] \qquad (34b)$$

This approximation was used by Nicolet for calculating the radiative transport in the entry environment (refs. 4 to 6). Since $E'_n(z) = -E_{n-1}(z)$, one could obtain the relation for the exponential integral of second order by differentiating equation (33) as

$$E_2(z) = \exp(-2z) \tag{35}$$

Use of equations (33) and (35) could be made directly in equations (24), (25a), and (25b) to obtain appropriate relations for the radiative heat flux.

In this study, use of the exponential kernel approximation, as given by equations (33) and (35), is made for the radiative transport in the shock layer. Furthermore, the bow shock is considered transparent, and the free stream is considered cold and transparent. For planetary entry conditions, radiative contribution from the body surface is usually neglected. However, it has been included in this study, and for a gray radiating surface it is obtained from equation (25a) as

$$q_R^+(0) = q_{R,w}^+ = \varepsilon_w \, \sigma^* \, T^{*4} \tag{36}$$

A value of surface emittance of $\varepsilon_w = 0.8$ is used in this study.

Spectral Models for Gaseous Absorption

Appropriate spectral models for gaseous absorption are needed for solution of the radiative flux equations. The absorption model considered in this study is for a nongray gas with continuum and line transitions. In general, the spectral absorption coefficient for continuum and line transitions may be expressed as

$$\kappa_\nu = \sum \kappa_i^C(\nu) + \sum \kappa_j^L(\nu) \tag{37}$$

The summations in the above equation extend over all continuum and line transitions respectively. In this study, only the transitions of the species H, H^-, and H_2 are considered.

The absorption coefficients for line transitions depend on the plasma conditions both through the population of the absorption levels and the shape of the spectral lines. For heavy atomic species at high temperatures, the dominant mechanism for the line broadening is the Stark broadening by electron impacts. Following Armstrong et al. (ref. 22), the lines can be treated as having the Lorentz shape, for which the shape factor is given by

$$b_k(\nu) = (\gamma_k^S/\Pi)/[(\nu - \nu_k)^2 + (\gamma_k^S)^2] \tag{38}$$

where ν_k is the frequency of the kth line center and γ_k^S is the Stark half-width of the line. In calculation of the absorption coefficients due to atomic line transitions, a line grouping technique is used. In this technique, line transitions near a specified frequency value are grouped together, and the spectral absorption is given as that from the line group. However, each line within the group is treated individually.

The continuum contribution depends mainly on the plasma state through the population of absorbing levels. The spectral absorption coefficient due to continuum transitions is given by

$$\kappa_i^C(\nu) = \sum N_{ij} \, \sigma_{ij}^C(\nu) \tag{39}$$

where N_{ij} is the number density of the absorbing level and σ_{ij}^C is its cross section. The number density of the particular particle is obtained from thermodynamic state calculations.

By employing detailed information on line and continuum absorption, Nicolet developed a fairly sophisticated radiative transport model for applications to planetary entry environment (refs. 4 to 6). The procedure for using this model is given in reference 5.

In the absorption model developed by Sutton (ref. 7), the frequency dependence of the absorption coefficient is represented by a step-function with 58 steps of fixed (but not necessarily equal) widths. In this model, the absorption of helium species is neglected. In step-function models, the total absorption coefficient of the jth step is a summation of the average absorption coefficient for the ith transition in the jth step, given by

$$\kappa_j(\omega) = \sum_i \kappa_{ij}(\omega) \tag{40}$$

$$\kappa_{ij}(\omega) = \frac{1}{\Delta\nu_j} \int_{\nu_j}^{\nu_j + \Delta\nu_j} \kappa_i(\omega) \, d\nu \tag{41}$$

$$\kappa_i = f(T, N_i, \nu) \tag{42}$$

Once again κ is the absorption coefficient, ν the frequency in eV, T is the temperature in degrees Kelvin, and N_i are the number density in cm^{-3}. In this model, the absorption coefficients for the free-free and bound-free transitions of atomic hydrogen are expressed by

$$\kappa_{ff}^H = (2.61 \times 10^{-35} N_e N_{H^+})/(T^{1/2} \nu^3) \tag{43}$$

$$\kappa_{bf}^H = \left[\frac{(1.99 \times 10^{-14} N_H)}{\nu^3}\right] \times \sum_{n_\ell=1}^{4} \left(\frac{1}{n_\ell^3}\right) \exp\left[\left(\frac{-157780}{T}\right)\left(1 - \left(\frac{1}{n_\ell^2}\right)\right)\right]$$

$$\text{for } 1 \leq n_\ell \leq 4 \tag{44}$$

and

$$\kappa_{bf}^H = \left[6.31 \times 10^{-20}\left(\frac{T}{\nu^3}\right) N_H\right] \exp(A) \left[\exp(B) - 1\right]$$

$$\text{for } 4 < N_\ell \leq N_{\ell max} \tag{45}$$

where

$$A = \left(\frac{-157780}{T}\right)\left[1 - \left(\frac{\delta}{13.6}\right)\right]$$

$$B = \left(\frac{157780}{T}\right)\left[\frac{1}{25} - \left(\frac{\delta}{13.6}\right)\right]$$

The reduction in the ionization potential δ is calculated by

$$\delta = (1.79 \times 10^{-5} \; N_e^{2/7})/T^{1/7} \qquad (46)$$

For bound-bound transition of hydrogen molecules and atoms

$$\kappa_{bb}^H = S \; b_k(\nu) \qquad (47)$$

where the line strength S is given by

$$S = (1.10 \times 10^{16} \; f \; n_\ell^2 \; N_H) \; \exp\left[\left(\frac{-157780}{T}\right) \left(1 - \left(\frac{1}{n_\ell^2}\right)\right)\right] \qquad (48)$$

The line-shape factor $b_k(\nu)$ is given by equation (38). Using the expressions given above, the absorption due to continuum and line transitions over each step is calculated individually. The total absorption over each individual step is a strong function of temperature, and this model is valid for a wide range of temperatures. Further information on the 58-step model is available in reference 7.

At high temperatures, the frequency dependence of the absorption coefficient is more orderly because of the relative importance of continuum transitions over line transitions. Under such conditions, it is possible to represent the spectral absorption of the gas by a relatively fewer number of steps. A spectral model consisting of 30 steps is introduced in this study to represent the absorption by the hydrogen species in the spectral range of 0 to 20 eV. The absorption by the helium species is also neglected in this study. The procedure for developing this model is to calculate the spectral absorption coefficient first by employing Nicolet's detailed model. This model calculates the absorption coefficients considering all possible transitions. It was mentioned before that the spectral absorption coefficient for a plasma consisting of a mixture of elements is in general the sum of continuum transitions and line transitions. The continuum transitions include atomic photo-ionization, photodetachment, free-free transitions, photodissociation and molecular photo-ionization. The hydrogen cross section for bound-free transitions is given by

16

$$\sigma_{bf} = \left[(2^6\Pi^4)/(3\sqrt{3})\right]\left[(me^{10}g_{bf})/(ch^6 n_a^5 \nu^3)\right] \tag{49}$$

and for free-free transitions by

$$\sigma_{ff} = (2^4\Pi^2 e^6 \, N_e \, g_{ff})/\left[3\sqrt{3} \; hc \; (2\Pi m)^{3/2}(kT)^{1/2}\nu^3\right] \tag{50}$$

where n_a is the principal quantum number of the absorbing level, N_e is the number density of free electrons, and g_{bf} and g_{ff} are Gaunt factors (ref. 4).

The absorption coefficients of the atomic line transitions are given as

$$\mu_k^L(j) = \left(\frac{\Pi e^2}{mc}\right) f_{k(j)} \, N_{ij} \, b_{k(j)} \tag{51}$$

where $f_{k(j)}$ is the oscillator strength of the kth line in the jth series of lines. The line-shape factor is expressed by equation (38). Hence, with this information, the total absorption coefficient is calculated as a detailed function of frequency. These results then are plotted on a convenient graph, and the frequency interval of each step, for the step model, is selected by inspection. The height of each step is determined by matching the area under the detailed model curve for the selected spectral interval. It is essential to provide a relatively larger number of steps in the spectral range of line radiation than continuum radiation. At present, it is necessary to obtain a different 30-step model for different entry conditions. This, however, could be avoided by establishing some kind of correlations between the results of step and detailed models. The method of approximating the absorption coefficient by the 30-step model is illustrated in figure 2 for 116-km entry conditions (ref. 12). Similar results were obtained for other entry conditions. It should be emphasized here that use of the step models replaces the integration over frequency intervals in the radiative flux equations by the summation over individual steps.

PHYSICAL CONDITIONS AND DATA SOURCE

The entry bodies considered for this study are a sphere cone of 55°
half-angle and a hyperboloid of 50° half-angle, both with a nose radius
of 22.2 cm. As mentioned earlier, the body surface is considered gray,
having a surface emittance of 0.8. The surface temperature is assumed to
be uniform at 4,200 K.

Information on Jupiter's atmospheric conditions is available in the
literature, and the free-stream conditions used in this study are summarized
in reference 12. The shock-layer gas is assumed to be a mixture of eight
chemical species, H_2, H, H^+, H^-, H_e, H_e^+, H_e^{++}, and e^-. The number densities
of these species are obtained by considering five chemical reactions. These
are discussed in references 7 and 12 where closed-form solutions for cal-
culating the number density are also provided. Thermodynamic properties for
specific heat, enthalpy, and free energy, and transport properties for
viscosity and thermal conductivity are required for each species. Relations
for calculating these properties are available in the literature, and these
are summarized in reference 12.

METHOD OF SOLUTION

The numerical procedure for solving the inviscid flow equations is de-
scribed in reference 10. The numerical procedure for solving the viscous
shock-layer equations is discussed in detail in references 10 and 12. In
essence, the numerical procedure for the viscous shock layer can easily be
adapted to the inviscid case. In the numerical procedure for viscous shock
layer, the variables of the governing equations are normalized with their
local shock values, and the transformed equations are written in a general
form as

$$\partial^2 W/\partial\eta^2 + c_1 \partial W/\partial\eta + c_2 W + c_3 + c_4 \partial W/\partial\xi = 0 \tag{52}$$

where $\eta = n/n_s$ and $\xi = s$. The quantity W represents $\bar{u} = u/u_s$ in the
s-momentum equation, $\bar{T} = T/T_s$ in the energy equation, and C_i in the
species continuity equation. The coefficients c_1 to c_4 are defined in

18

reference 10. The second-order partial differential equations, as expressed
by equation (52), are solved by employing an implicit finite-difference
method. A variable grid-spacing central difference equation is used in
the normal direction and equal spacing forward difference equation in the
tangential direction. The details of the numerical procedure are given
in references 10 and 12.

RESULTS AND DISCUSSION

By employing the three radiative transport models discussed under
"Radiation Models," results were obtained for temperature, pressure, density,
shock standoff distance, and radiative flux distribution in the shock layer
and along the body surface for different entry conditions and body configura-
tions. Inviscid as well as viscous results were obtained for a 55° half-
angle sphere cone, while only viscous results were obtained for a 50° hyper-
boloid. In this section a comparison of inviscid and viscous results is
presented for a 55° sphere cone entering the Jovian atmosphere at an alti-
tude of z = 116 km, followed by a series of viscous results for the 55°
sphere cone at different entry conditions. Finally, viscous results for
a 50° hyperboloid are presented.

Comparison of Inviscid and Viscous Results

Inviscid and viscous results obtained by employing the detailed and 30-
step radiation models are compared in this section. The temperature distribu-
tion along the stagnation streamline is illustrated in figure 3. The agreement
between inviscid and viscous results is seen to be fairly good except near
the body, where viscous boundary-layer effects are predominant (see fig. 3b).
The difference between the detailed and 30-step model results is lower for
the inviscid case than the viscous case. This is due to relatively higher
temperature across the shock layer for the inviscid analysis. As pointed
out earlier, the step model is more accurate at higher temperatures.

The shock standoff distance as a function of body location is illustrated
in figure 4. The first three curves illustrate the inviscid results for the
three different radiation models. The fourth curve, obtained by employing

Nicolet's detailed radiation model, is for the viscous case, and is drawn here for comparison. The shock standoff distance is slightly larger for the present 30-step model as compared with the results of the detailed and Sutton's 58-step models. Although the difference between inviscid and viscous results is seen to be quite small, use of the viscous analysis is recommended for more realistic and accurate calculations.

Results of radiative heating along the body are illustrated in figure 5. While inviscid results are seen to be slightly higher at the stagnation point, viscous results are relatively higher at other body locations (up to $s/R_N = 0.6$). This is a direct consequence of viscous boundary-layer effects. Discussion on viscous results of different radiation models is given in the next subsection.

Viscous Results for a 55° Sphere Cone

Viscous results for a 55° sphere cone (with a nose radius of 22.2 cm) is presented in this subsection for different entry conditions. Results of various radiation models are compared in order to establish the validity of the present 30-step radiation model.

In the shock layer, the temperature distribution along the stagnation streamline is illustrated in figure 6 for two different free-stream (density) conditions. It is found that the present 30-step model underpredicts the shock-layer temperature by a maximum of 11 percent in comparison to Nicolet's detailed model and by about 4.5 percent when compared with Sutton's 58-step model. For free-stream conditions resulting in higher shock temperature, the agreement between the results is even better. This is because the higher temperature absorption spectrum can be approximated accurately by the present step-model.

From the results presented in figures 3 and 6, it is noted that there exists a steep temperature gradient in the regions close to the body. At locations about five times the nose radius (normal to the body), only a slight variation in the shock-layer temperature is noticed. This fact was utilized in dividing the shock layer into different temperature zones for evaluating the absorption coefficient. In a preliminary study, two methods were used to account for the temperature dependence of the absorption coefficient. In

the first method, the absorption coefficient was calculated at the shock temperature, T_s^*. This value was used in analyzing the flow field in the entire shock layer. Results obtained by this method are designated here as "present-approximate" results. In the second method, the shock layer is divided into three different temperature zones, two of which are closer to the body (because of the steep gradient near the body). For each temperature zone, a different 30-step model for absorption is obtained. These are read as input in the computer program while evaluating the flow variables in the particular temperature zone. Results obtained by this method are denoted here as "present" results.

The variation in temperature just behind the shock (at location $n = 0.05$) with distance along the body surface is illustrated in figure 7 for entry conditions at $z = 116$ km. The results of the present model are found to be about six percent lower than the results of Nicolet's model. This difference is seen to be fairly uniform along the body.

The pressure distribution along the body is illustrated in figure 8 for two different entry conditions ($z = 116$ and 131 km). The results show the same general trend as exhibited by figure 7 for temperature distribution. However, the agreement between the results is better for pressure distribution.

The variation in density just behind the shock ($n = 0.05$) with distance along the body is illustrated in figure 9 for entry conditions at $z = 116$ km. The present model is seen to underestimate the density by a maximum of nine percent as compared with the results of Nicolet's model.

Figure 10 shows the shock standoff variation with distance along the body surface for entry conditions at $z = 116$ km. Results of Sutton's model are found to be in general agreement with the results of Nicolet's model. The present model is seen to overestimate the results by a maximum of 8.6 percent when compared with the results of Nicolet's model. This is mainly because the present model underpredicts the shock-layer density.

The radiation heating rate along the body surface is illustrated in figures 11 and 12 for different entry conditions. As would be expected, in all cases, the maximum heating occurs at the stagnation point. For $z = 116$ km, results presented in figure 11 show that the present model underpredicts the heating rate by a maximum of 13.6 percent when compared with Nicolet's model.

For the case of higher free-stream density (and hence a higher shock temperature), differences in the results of the present and other models are seen to be smaller. Figure 12 shows the results of radiative heating for 131-km entry conditions. For this higher altitude, the heat transferred to the body is lower because of lower free-stream density and pressure. For this case, differences in the results of the present and Nicolet's model are seen to be slightly higher.

Viscous Results for a 50° Hyperboloid

Viscous results for a 50° hyperboloid (with a nose radius of 22.2 cm) are presented in this subsection for different entry conditions. The temperature distribution in the shock layer (along the stagnation streamline) is illustrated in figure 13 for entry conditions at $z = 116$ km. The results of the three radiation models are seen to follow the same general trend as for the 55° sphere cone. A maximum difference of about 4.5 percent is seen between the present model and Nicolet's model. This difference is near the body (at $n = 0.0095$). Agreements between the results are better towards the shock.

The variation in temperature just behind the shock (at location $n = 0.07$) with distance along the body surface is illustrated in figure 14 for entry conditions at $z = 116$ km. The results indicate very good agreement between the three radiation models. The results of the present model are within 1.4 percent of the results of Nicolet's model. As would be expected, maximum difference in results occurs at the stagnation streamline.

The pressure distribution along the tangential coordinate is shown in figure 15 for two locations ($n = 0.002$ and 0.07) and for entry conditions at $z = 116$ km. The results obtained by using the present and Nicolet's radiation models are found to be in good agreement for both locations. The difference between the two results is less than one percent. The pressure distribution along the tangential coordinate (at $n = 0.001$) is shown in figure 16 for entry conditions at $z = 131$ km. The results indicate no significant difference between the results of the present and Nicolet's models. These results indicate that the pressure variation in the shock layer is relatively insensitive to the radiation models.

The variation in density just behind the shock (n = 0.07) with distance
along the body is illustrated in figure 17 for entry conditions at z = 116 km.
A maximum difference of about 6.5 percent is noted between results of the
present and Nicolet's model. The maximum difference in results of the present
and Sutton's models is about 3 percent.

The shock standoff variation with distance along the body surface for
entry conditions at z = 116 km is shown in figure 18. As was the case with
the 55° sphere cone, the present model is seen to overestimate the results
in comparison to the other models.

The radiative heating rate along the body surface is illustrated in figures
19 to 21 for different entry conditions. For this body geometry also, the
maximum heating occurs at the stagnation point. For z = 116 km, results
presented in figure 19 indicate that the present model underpredicts the
heating rate by a maximum of about 13 percent when compared with Nicolet's
model. For higher free-stream density, the results presented in figure 20
show smaller differences in the results of various radiation models. For entry
conditions at z = 131 km, results presented in figure 21 indicate that
heat transferred to the body is significantly lower. This is because of lower
free-stream density and pressure. As was the case with the 55° sphere cone
at this altitude, the difference between the present and Nicolet's results
is relatively higher.

CONCLUSIONS

A simple, nongray radiation model (a 30-step model) has been introduced
to investigate the flow phenomena in the viscous, radiating shock layer of
a Jovian entry body. Results obtained by this model are found to be in
general agreement with the results of Sutton's 58-step model and Nicolet's
detailed model. In most cases (except for the shock standoff distance), the
present model is found to underestimate the results in the shock layer as well
as along the body. The differences in results are lower for conditions re-
sulting in higher shock temperatures. The pressure variation is found to be
insensitive to the variation in radiation models.

It is found that use of the present model reduces the computational time significantly. The use of this simplified model is recommended for general parametric studies. It is suggested that some kind of correlation be developed to relate the absorption spectrum of the present model with that of Nicolet's detailed model. A correlation like this would make the present model more accurate and versatile.

REFERENCES

1. Anderson, J.D.: An Engineering Survey of Radiating Shock Layers. AIAA, Vol. 7, No. 9, Sept. 1969, pp. 1665-1675.

2. Olstad, W.B.: Nongray Radiating Flow About Smooth Symmetric Bodies. AIAA, Vol. 9, No. 1, Jan. 1971, pp. 122-130.

3. Callis, L.B.: Coupled Nongray Radiating Flow About Long Blunt Bodies. AIAA, Vol. 9, No. 4, April 1971, pp. 553-559.

4. Nicolet, W.E.: Advanced Methods for Calculating Radiation Transport in Ablation. Product Contaminated Boundary Layers. NASA CR-1656, Sept. 1970.

5. Nicolet, W.E.: Users Manual for RAD/EQUIL/1973, A General Purpose Radiation Transport Program. NASA CR-132470, 1973.

6. Nicolet, W.E.: Rapid Methods for Calculating Radiation Transport in the Entry Environment. NASA CR-2528, April 1975.

7. Sutton, K.: A 58-Step Radiation Model for Absorption by Hydrogen Species. (Unpublished work.) Also, Zoby, E.V.; Sutton, K.; Olstad, W.B.; and Moss, J.N. An Approximate Inviscid Radiating Flow Field Analysis for Outer Planet Entry Probes. AIAA Paper No. 78-189, Jan. 1978.

8. Sutton, K.. Characteristics of Coupled Nongray Radiating Gas Flows with Ablation Product Effec' ، About Blunt Bodies During Planetary Entries. Ph.D. Dissertation, North Carolina State Univ. (Raleigh), 1973.

9. Hughes, W.F.; and Gaylord, E.W.: B.sic Equations of Engineering Science. Schaum Publishing Company (New York), 1964.

10. Moss, J.N.: Reacting Viscous-Shock-Layer Solutions with Multicomponent Diffusion and Mass Injection. NASA TR R-411, June 1974.

11. Moss, J.N.: Radiative Viscous-Shock-Layer Solutions with Coupled Ablation Injection. AIAA, Vol. 14, No. 9, Sept. 1976, pp. 1311-1316.

12. Tiwari, S.N.; and Szema, K.Y.: Influence of Precursor Heating on Viscous Flow Around a Jovian Entry Body. AIAA Paper No. 78-1970, Jan. 1978. Also, NASA Technical Report NAS1-14193-27, School of Engineering, Old Dominion Univ. (Norfolk, Va.), Sept. 1978.

13. Zoby, E.V.; Gnoffo, P.A.; and Graves, R.A.: Correlations for Determining Thermodynamic Properties of Hydrogen-Helium Gas Mixtures at Temperatures from 7,000 to 35,000 K. NASA TN D-8262, Aug. 1976.

14. Kennet, H.; and Strack, S.L.: Stagnation Point Radiative Heat Transfer. ARS J., Vol. 31, No. 3, 1961, pp. 370-372

15. Hoshizaki, H.; and Lasher, L.E.: Convective and Radiative Heat Transfer to an Ablating Body. AIAA, Vol. 6, No. 8, 1968, pp. 1441-1449.

16. Chien, Kuei-Yuan: Application of the S_n Method of Spherically Symmetric Radiative-Transfer Problems. AIAA Paper No. 71-466, 1971.

17. Wilson, K.H.: Evaluation of One-Dimensional Approximations for Radiative Transport in Blunt Body Shock Layers. LMSC N-EE-71-3, Lockheed Missiles and Space Co. (Sunnyvale, Calif.), 1971.

18. Page, W.A.: Aerodynamic Heating for Probe Vehicles Entering the Outer Planets. AAS Paper No. AAS-71-144, 1971.

19. Vincenti, W.G.; and Kruger, C.H.: Introduction to Physical Gas Dynamics. John Wiley and Sons, 1965.

20. Sparrow, E.M.; and Cess, R.D.: Radiation Heat Transfer. Brooks/Cole Publishing Co. (Belmont, Calif.), 1966.

21. Hunt, B.L.; and Sibulkin M.: Radiation Transfer in a Gas of Uniform Properties in Local Thermodynamic Equilibrium. Part I, Part II, and Part III, Brown Univ., Report No. NONR-562(35)/18, 1966.

22. Armstrong, B.H.; Johnston, R.R.; and Kelly, P.S.: Opacity of High Temperature Air. Lockheed Missiles & Space Co., Report No. 8-94-64-2 (also Air Force Weapons Lab, Report AFWL-tr 65-17), 1964.
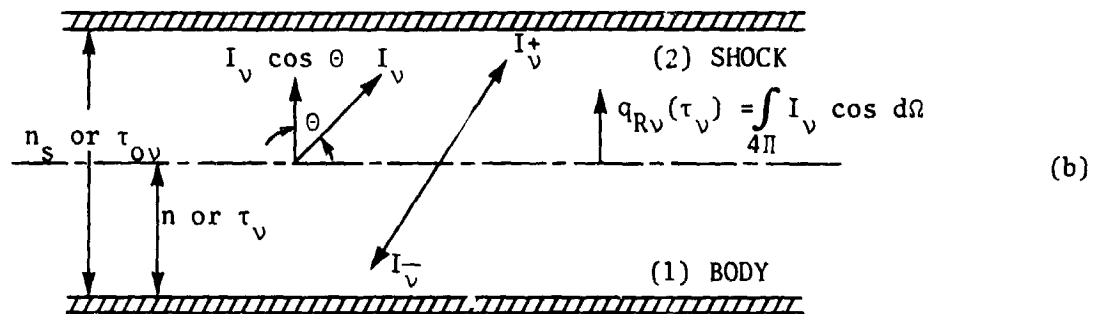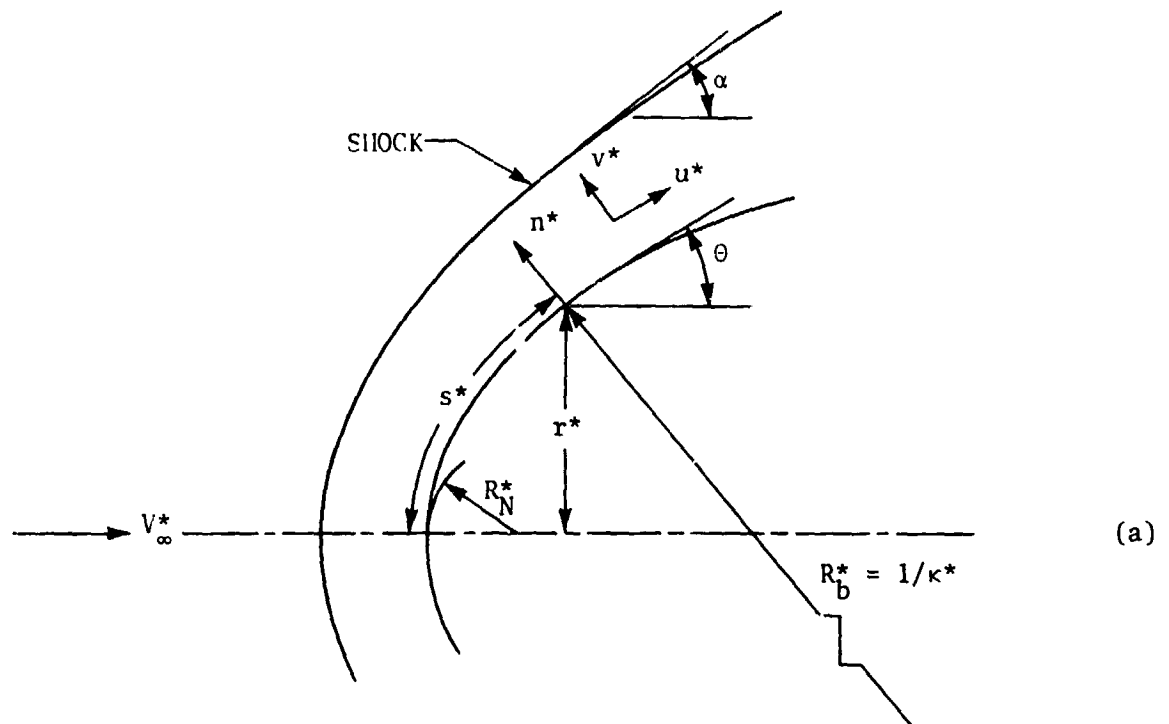
Figure 1. Physical model and coordinate system.
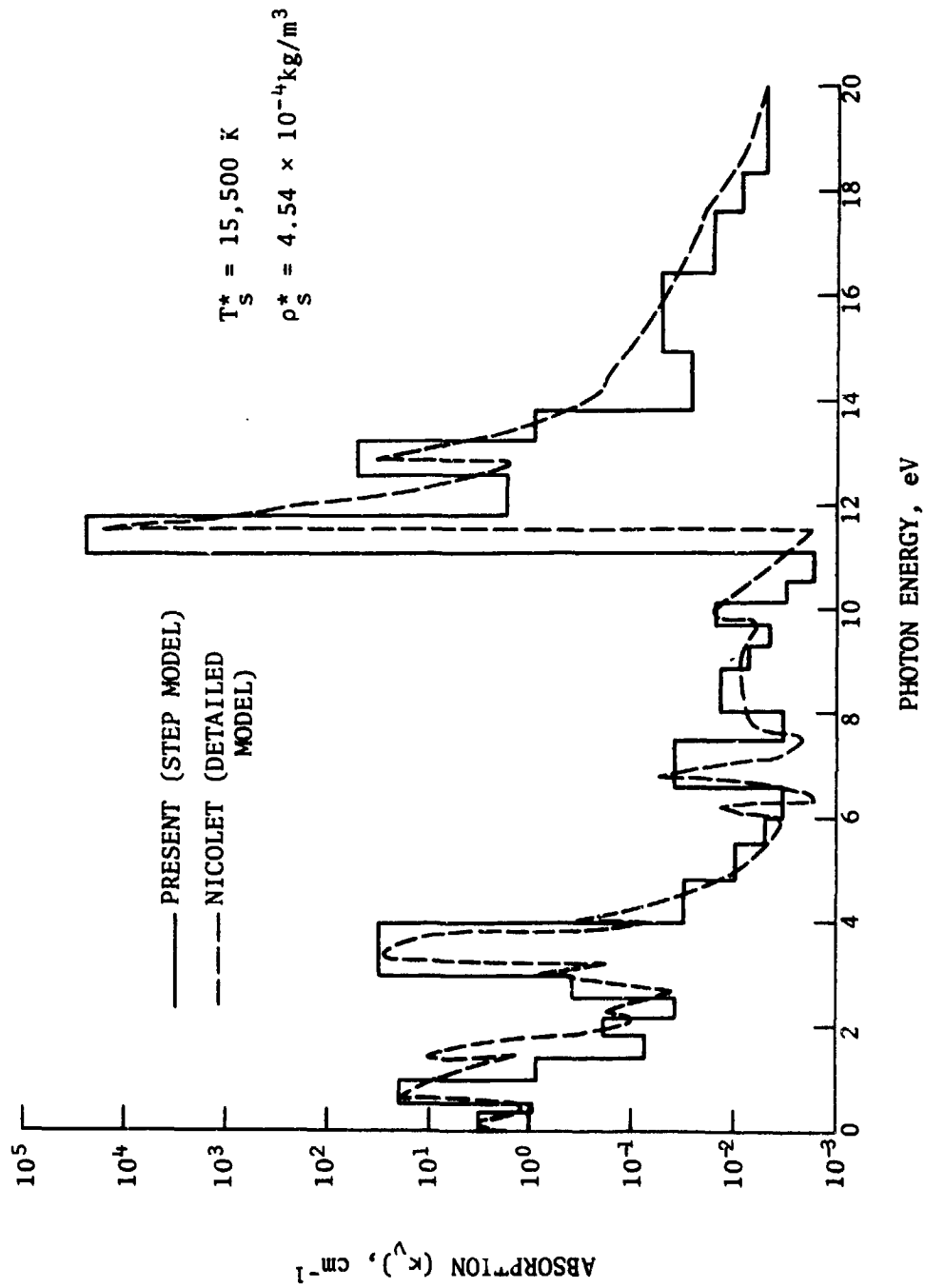
Figure 2. A 30-step model to approximate the absorption by Nicolet's detailed model (T_s = 15,500 K).

28
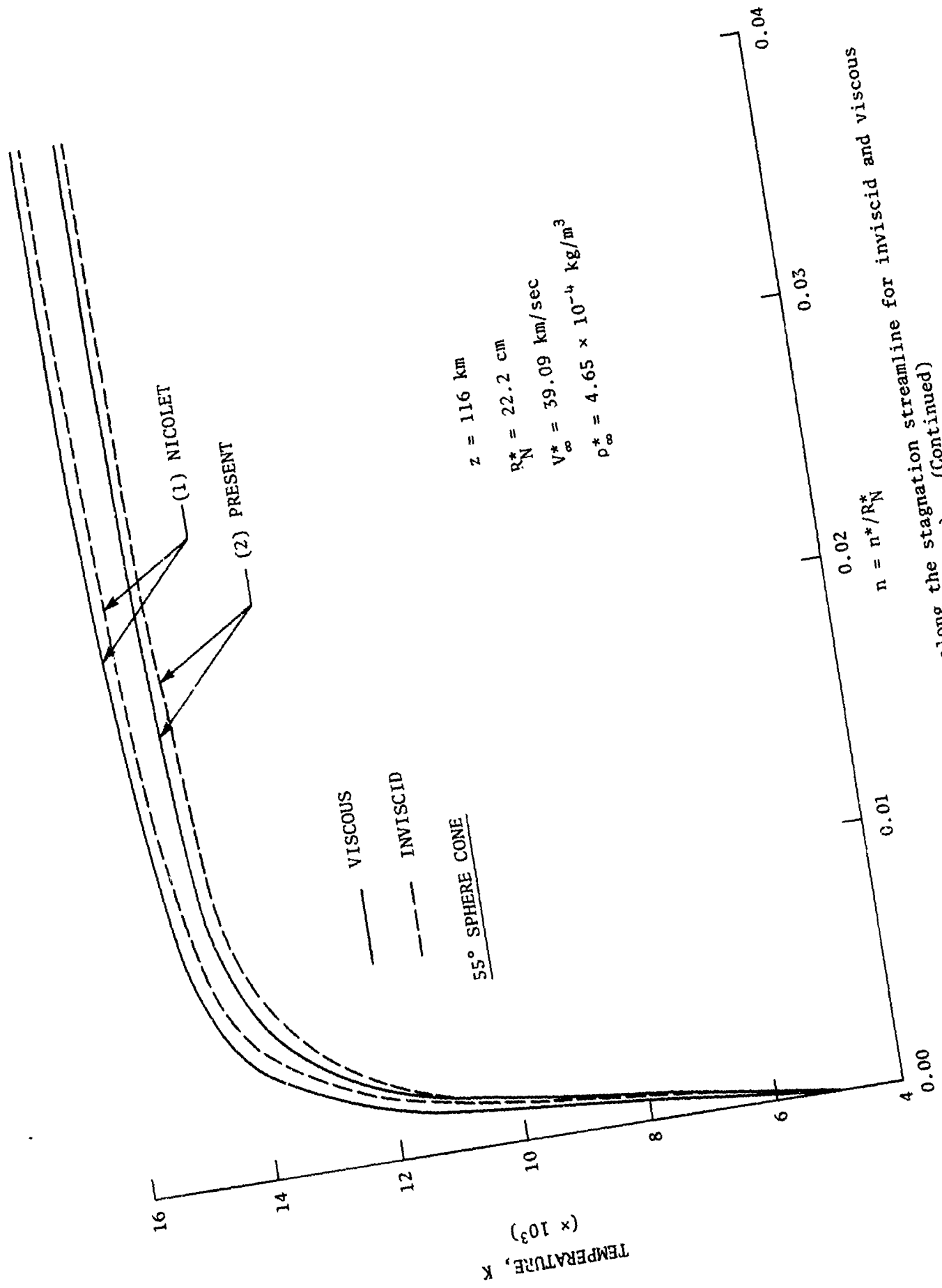
Figure 3. Temperature distribution along the stagnation streamline for inviscid and viscous analysis (55° sphere cone, z = 116 km). (Continued)

29
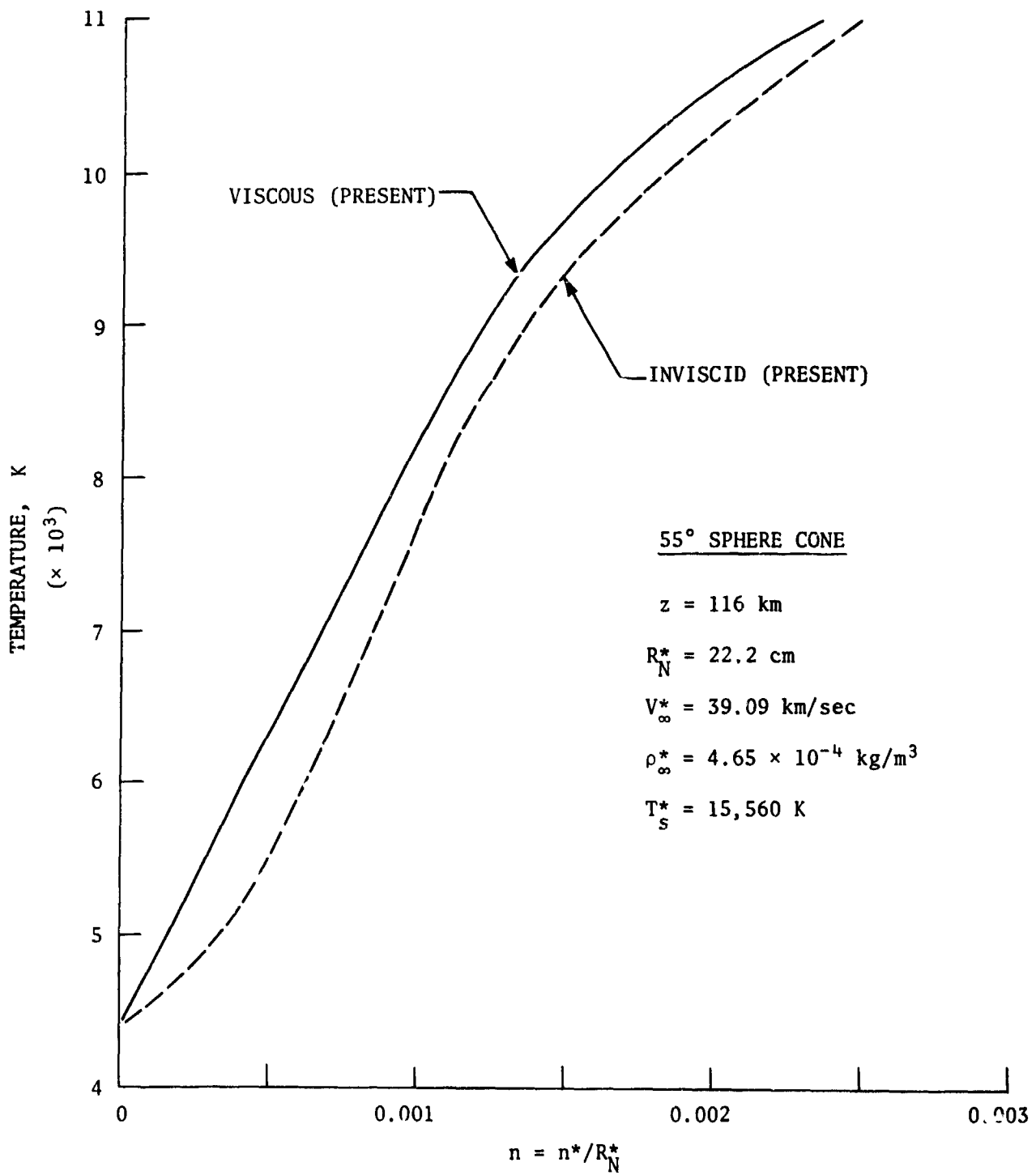
Figure 3. (Concluded)
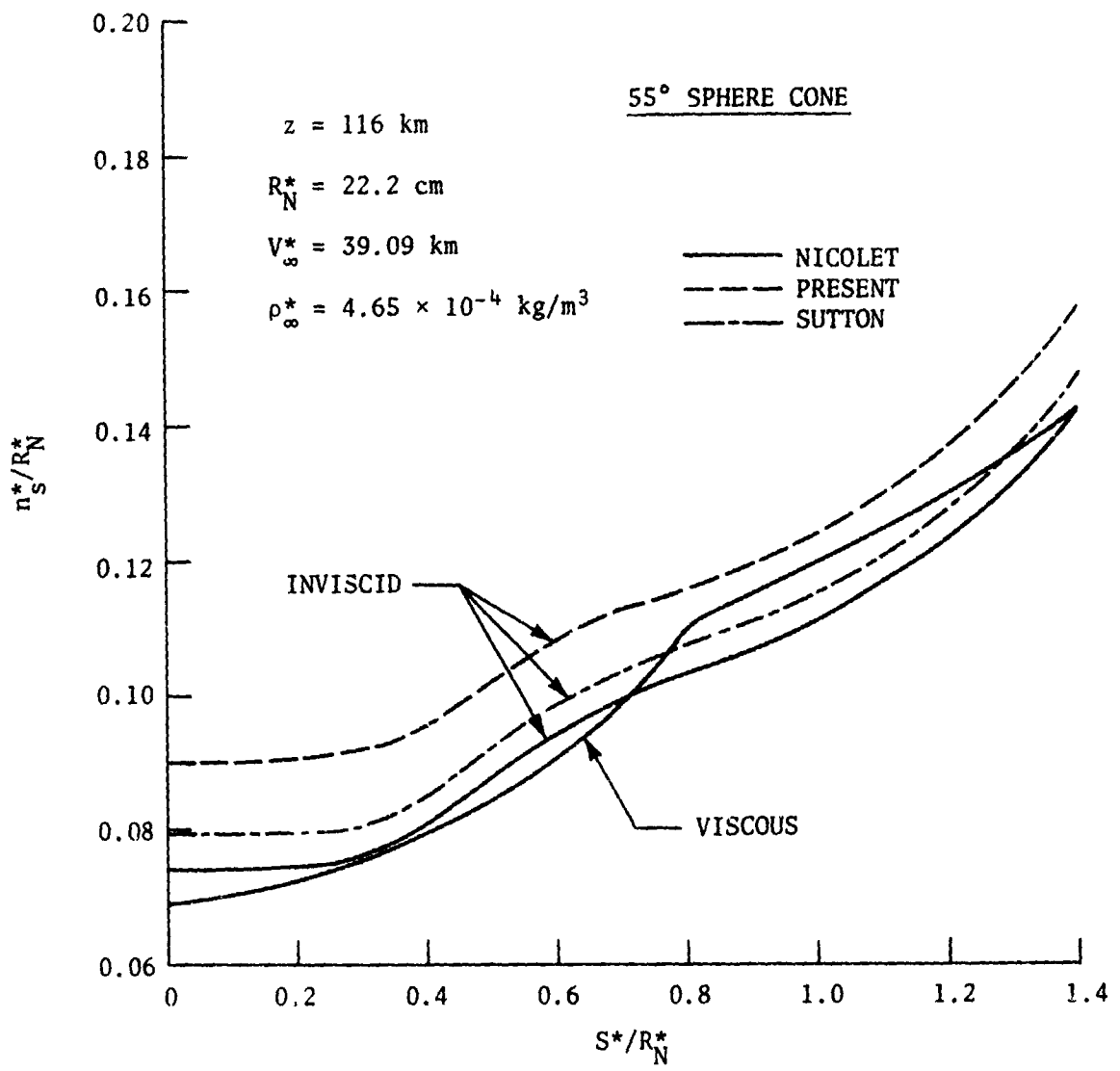
Figure 4. Shock standoff variation with distance along the body surface for inviscid and viscous analysis (55° sphere cone, z = 116 km).
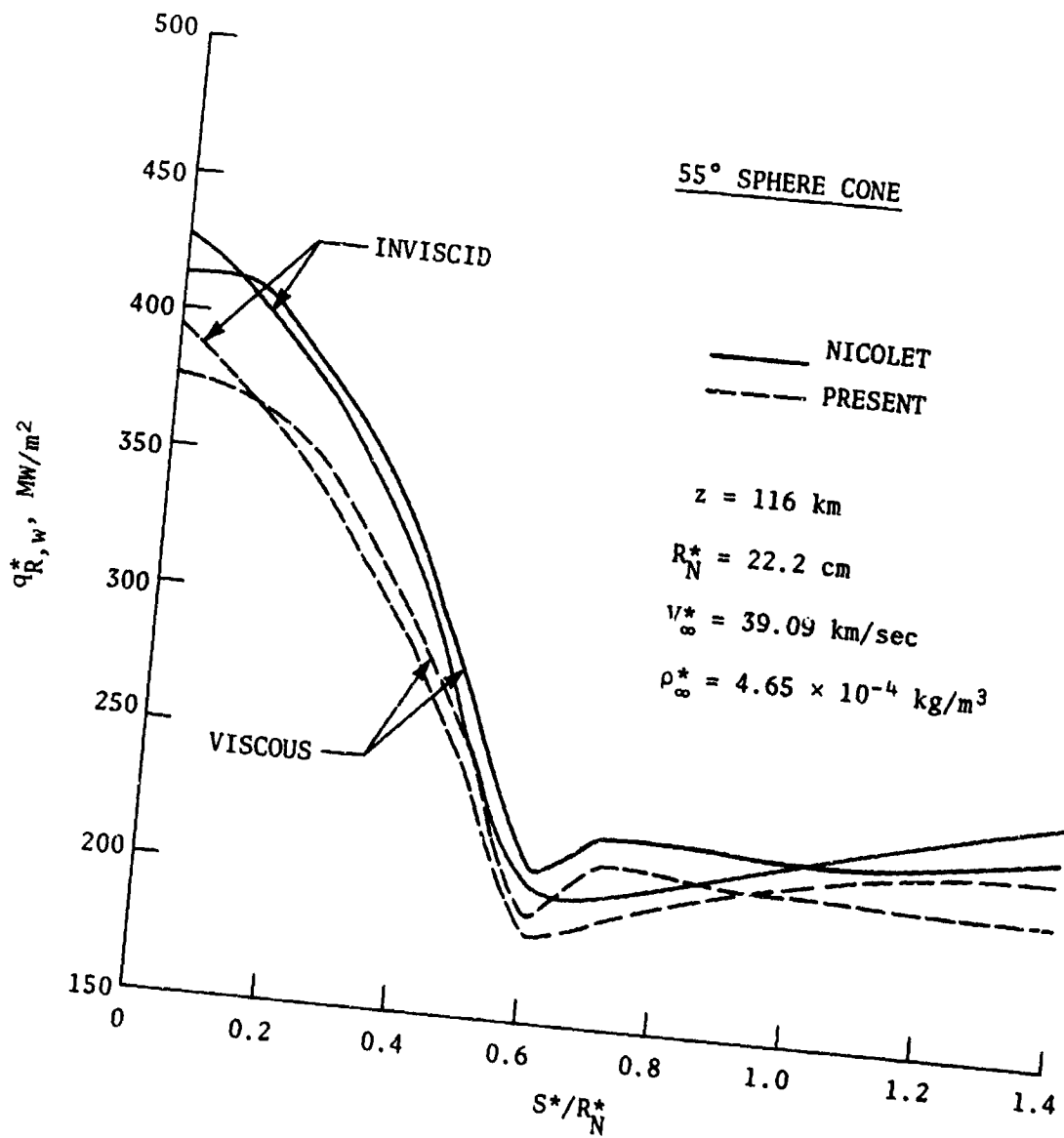
Figure 5. Radiative heating along the body for inviscid
and viscous analysis (55° sphere cone, z = 116 km).
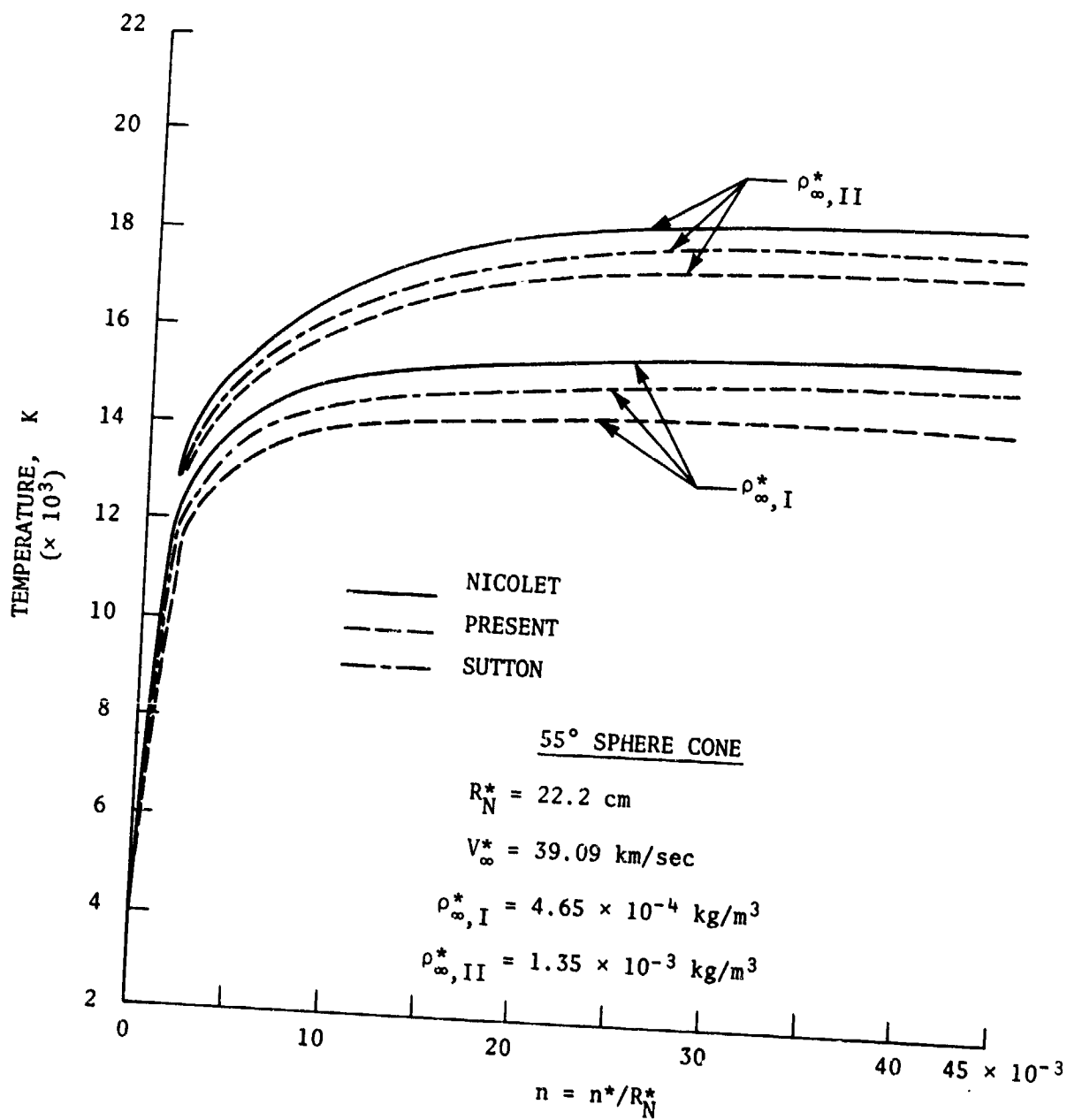
Figure 6. Temperature distribution along the stagnation streamline for two different free-stream densities (55° sphere cone).
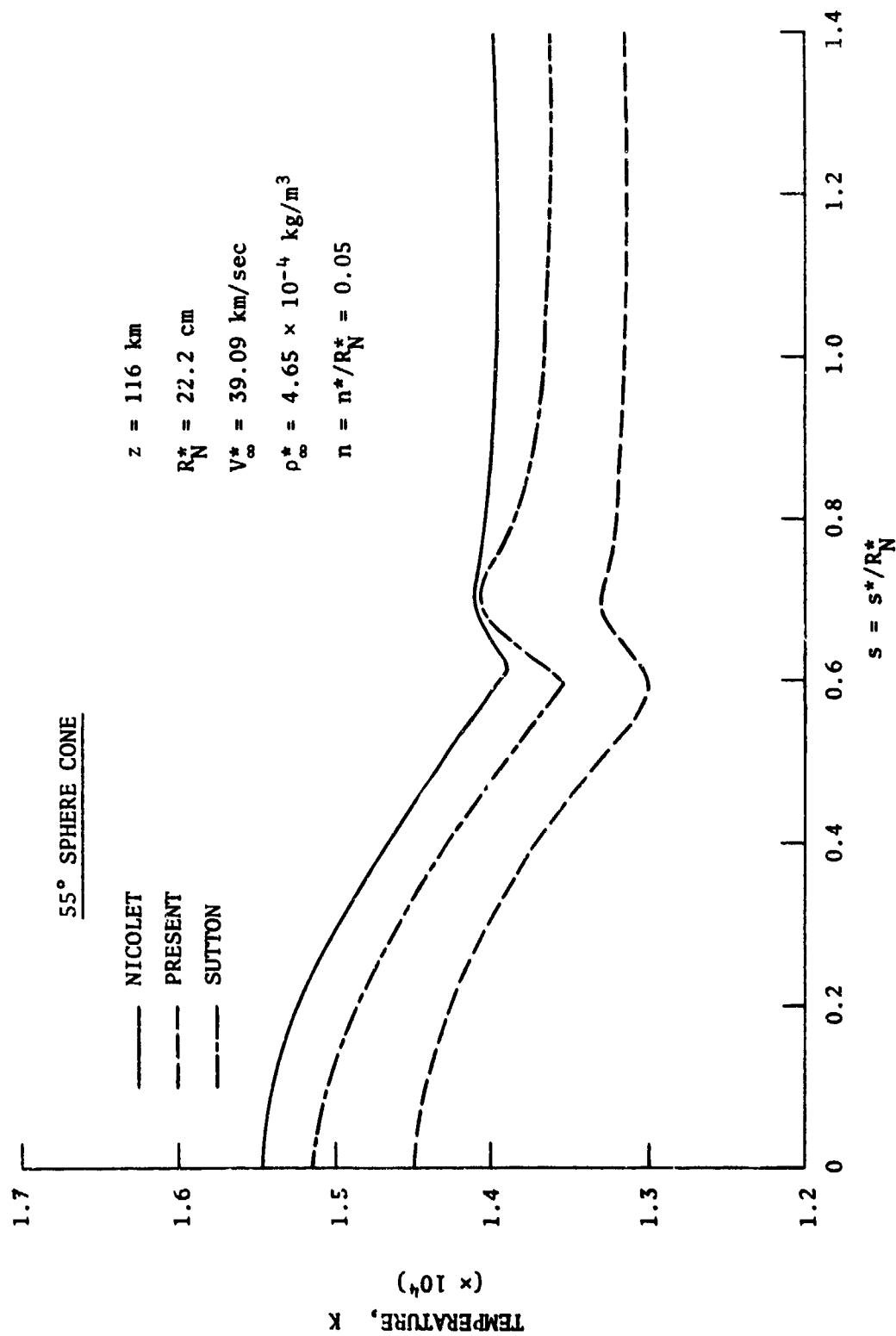
Figure 7. Temperature variation just behind the shock (n = 0.05) with distance along the body surface (55° sphere cone, z = 116 km).
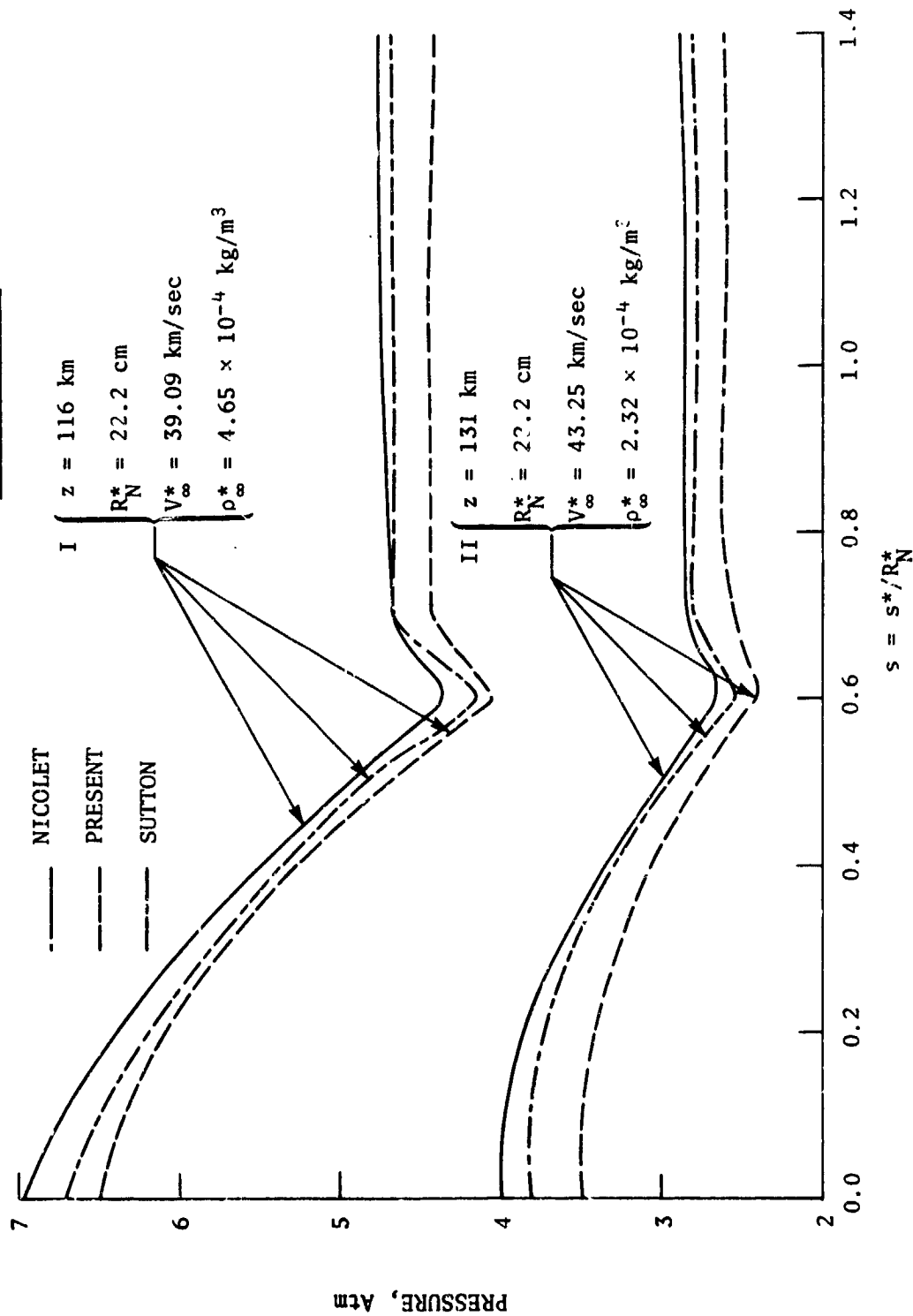
Figure 8. Pressure distribution along the body for two different entry conditions (55° sphere cone).
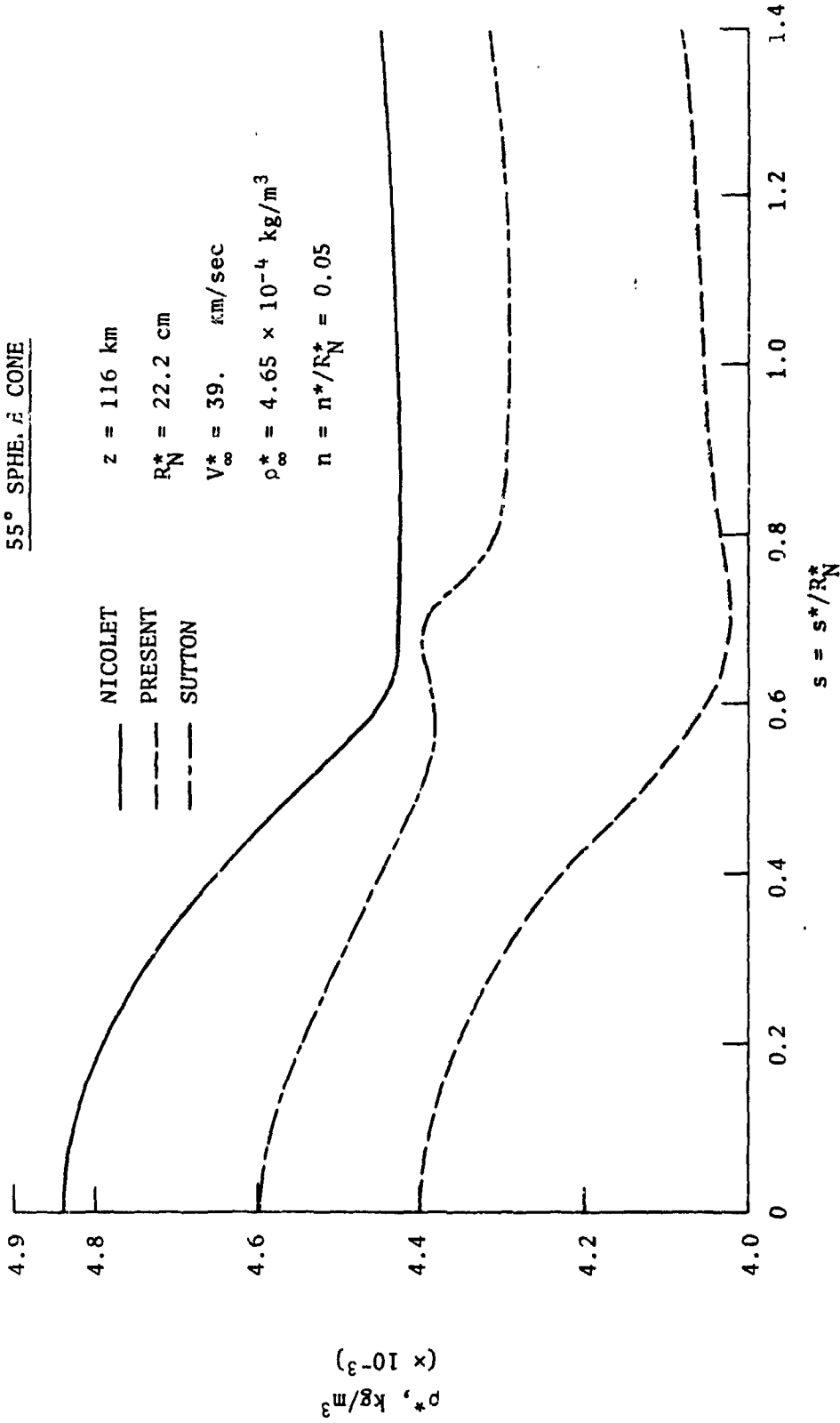
Figure 9. Density variation behind the shock ($n = 0.05$) with distance along the body surface (55° sphere cone, $z = 116$ km).

36
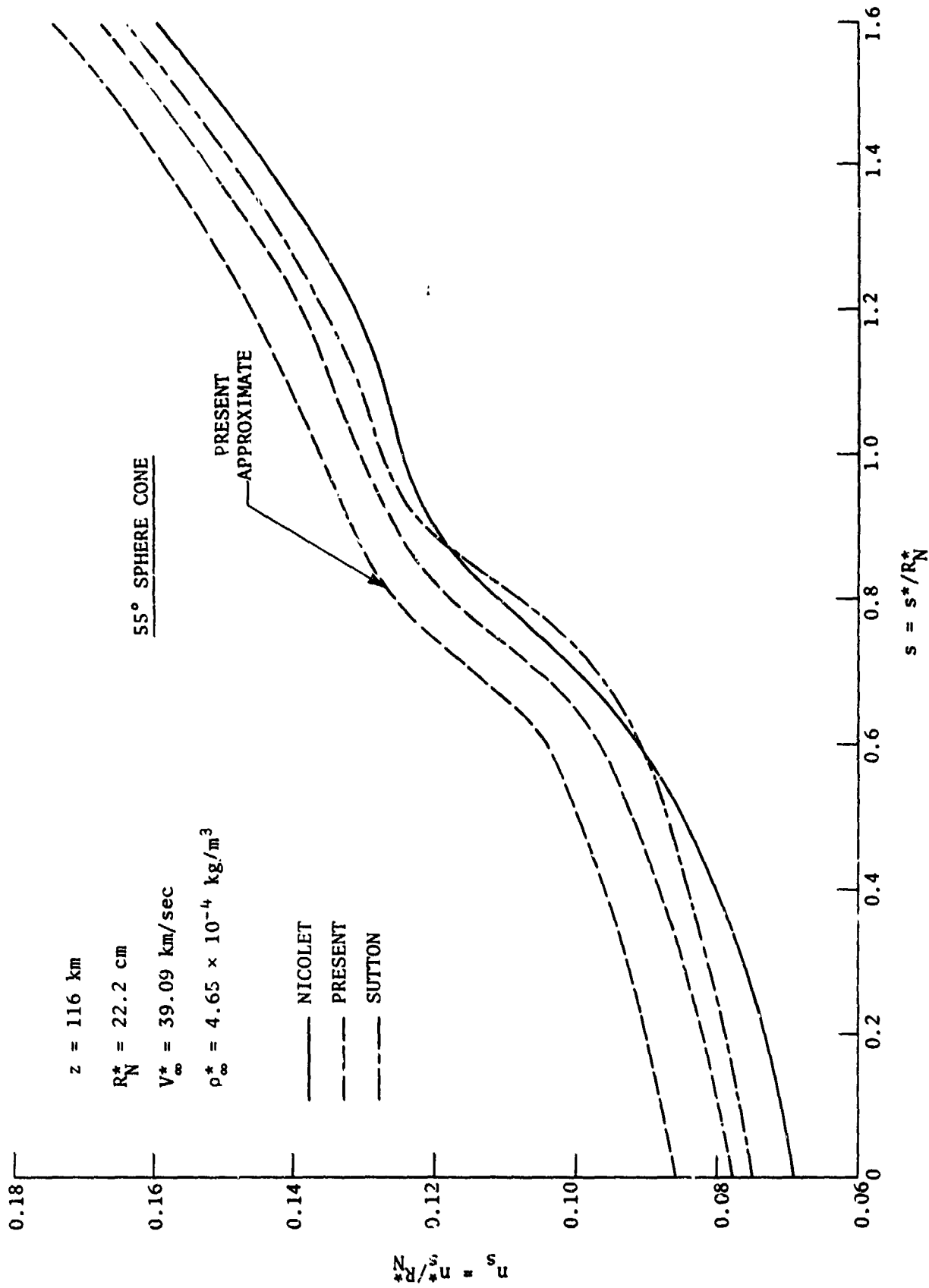
Figure 10. Shock standoff variation with distance along the body surface (55° sphere cone, z = 116 km).

37
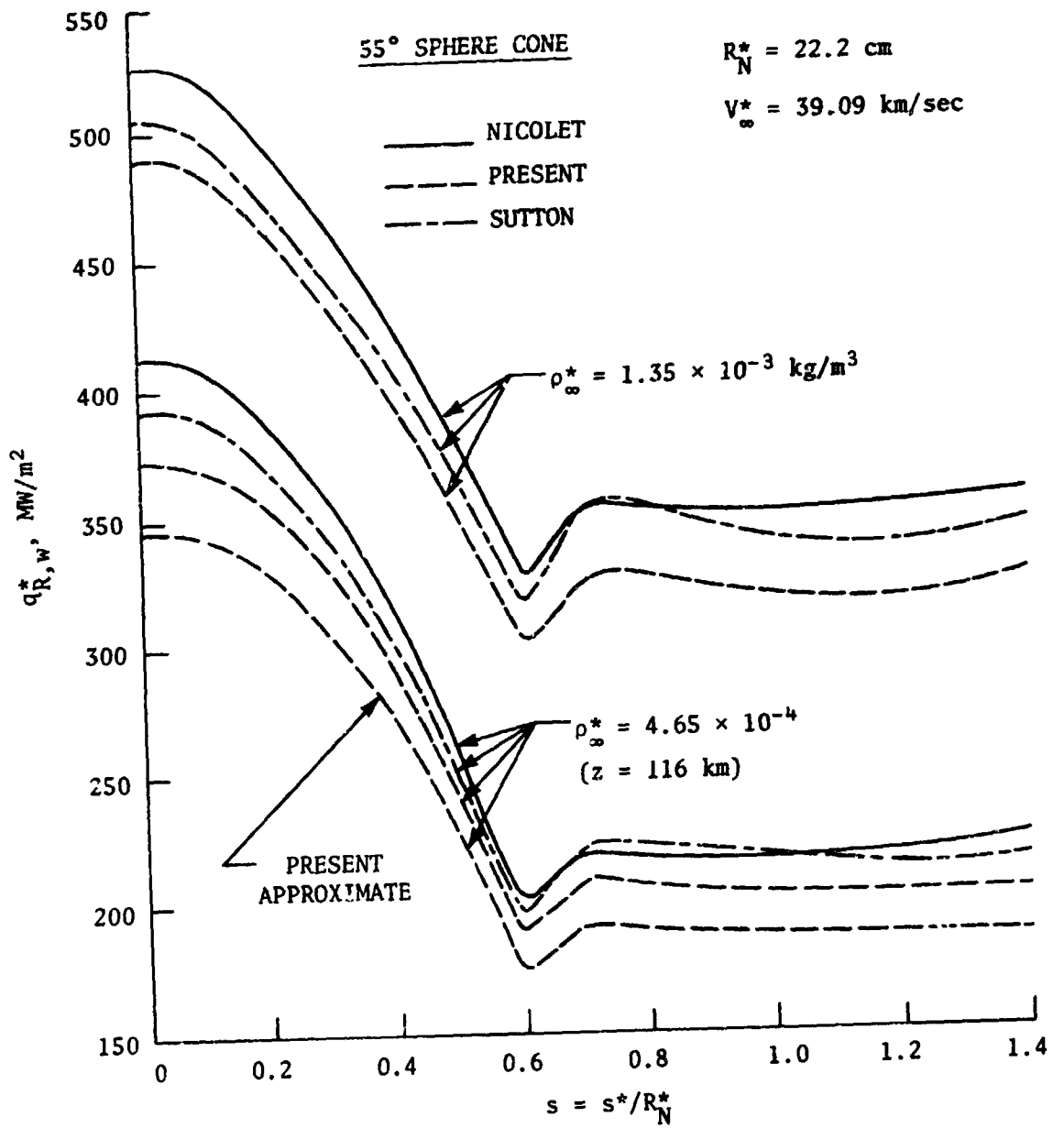
Figure 11. Radiative heating along the body for two different free-stream densities (55° sphere cone).
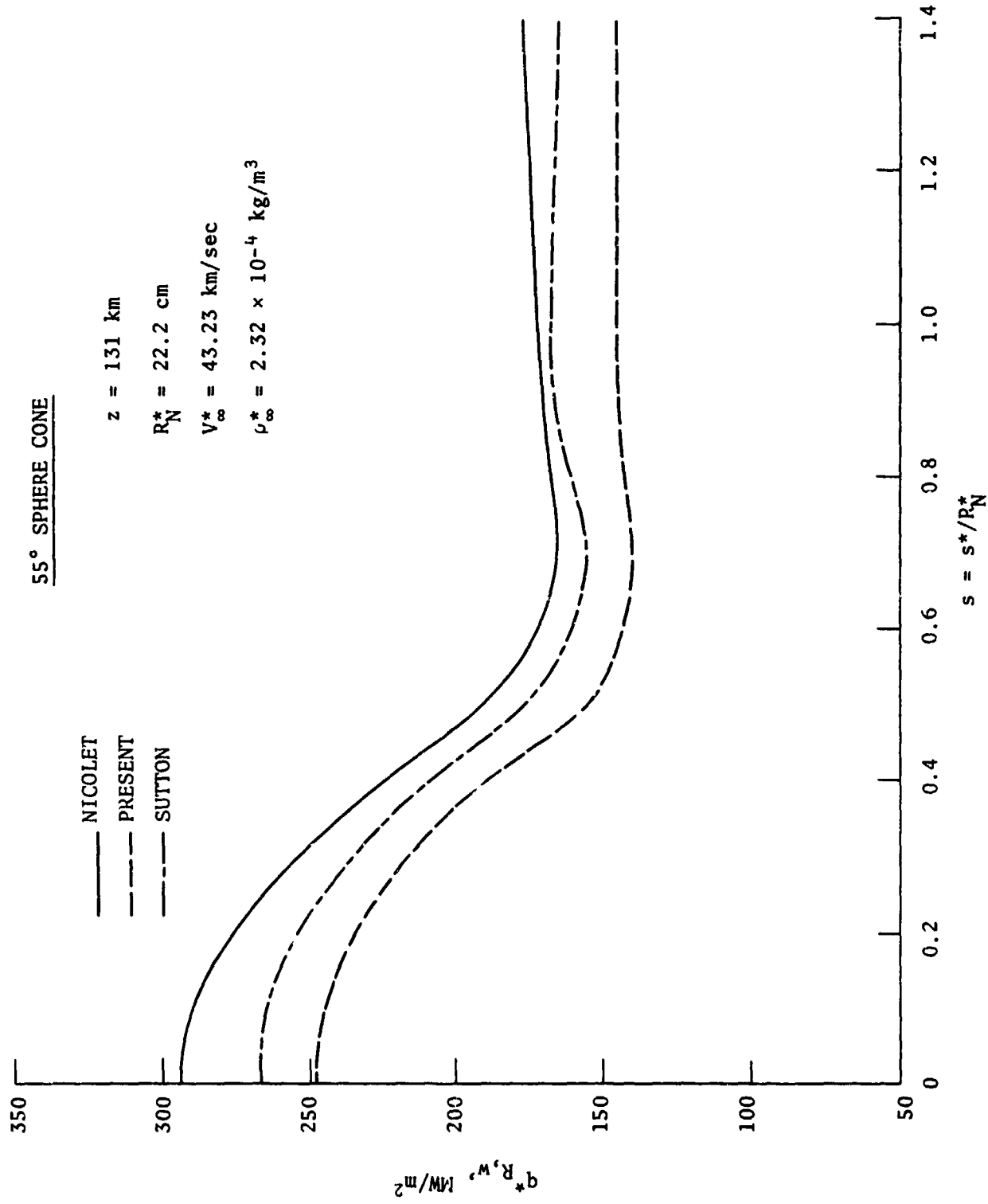
Figure 12. Radiative heating along the body for entry conditions at z = 131 km (55° sphere cone).

39
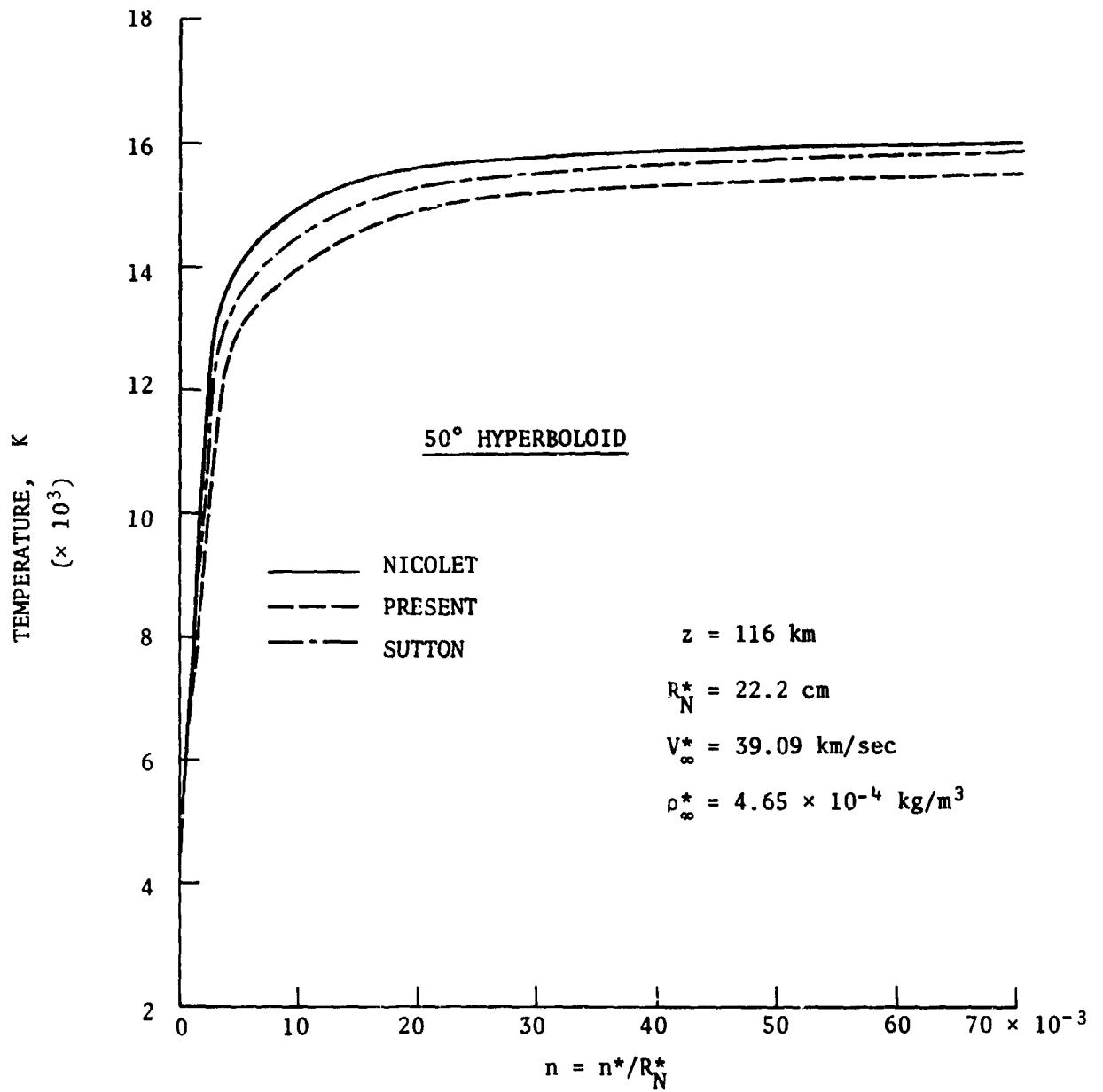
Figure 13. Temperature distribution along the stagnation
streamline (50° hyperboloid, z = 116 km).
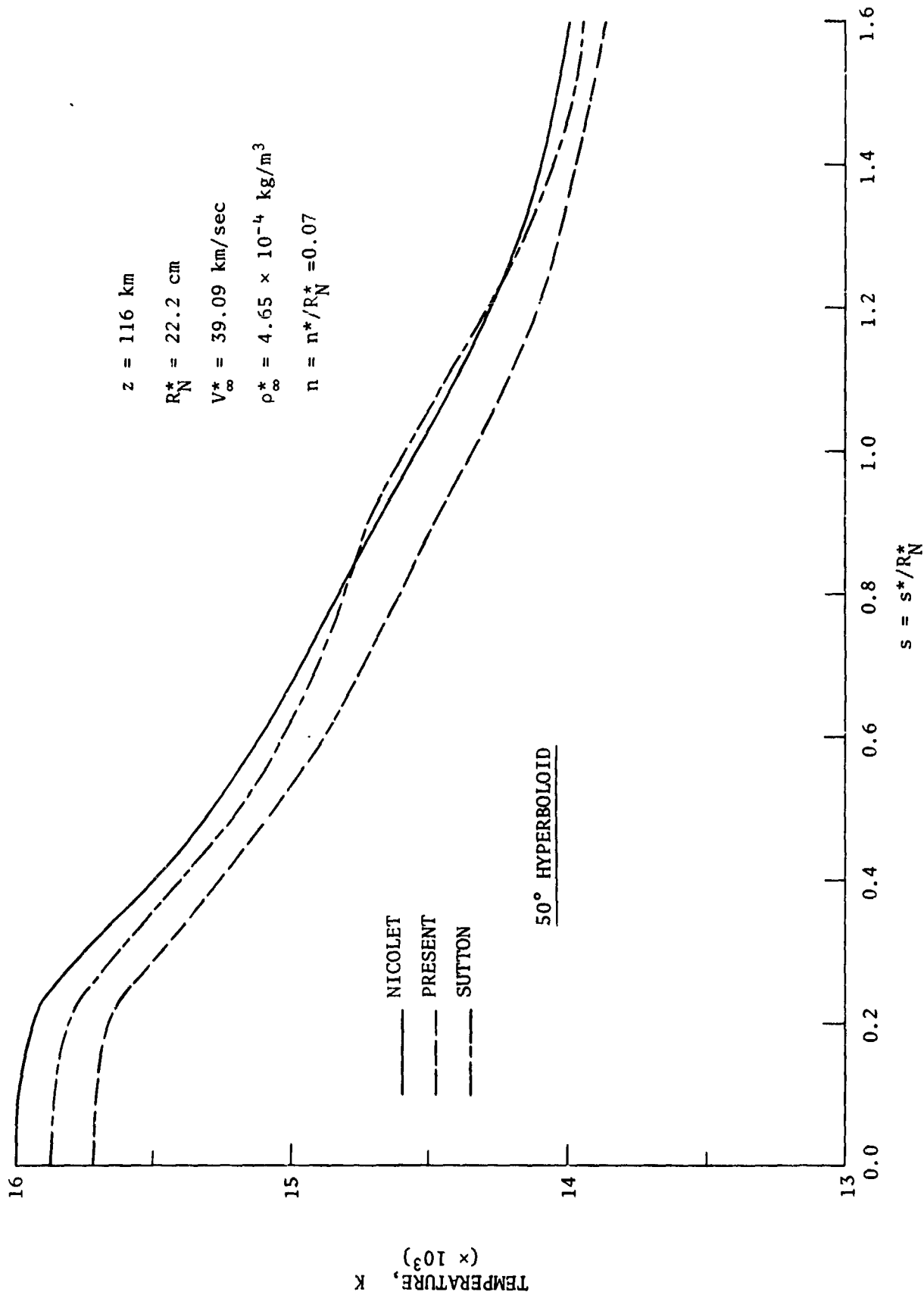
Figure 14. Temperature distribution just behind the shock (n = 0.07) with distance along the body surface (50° hyperboloid, z = 116 km)

41
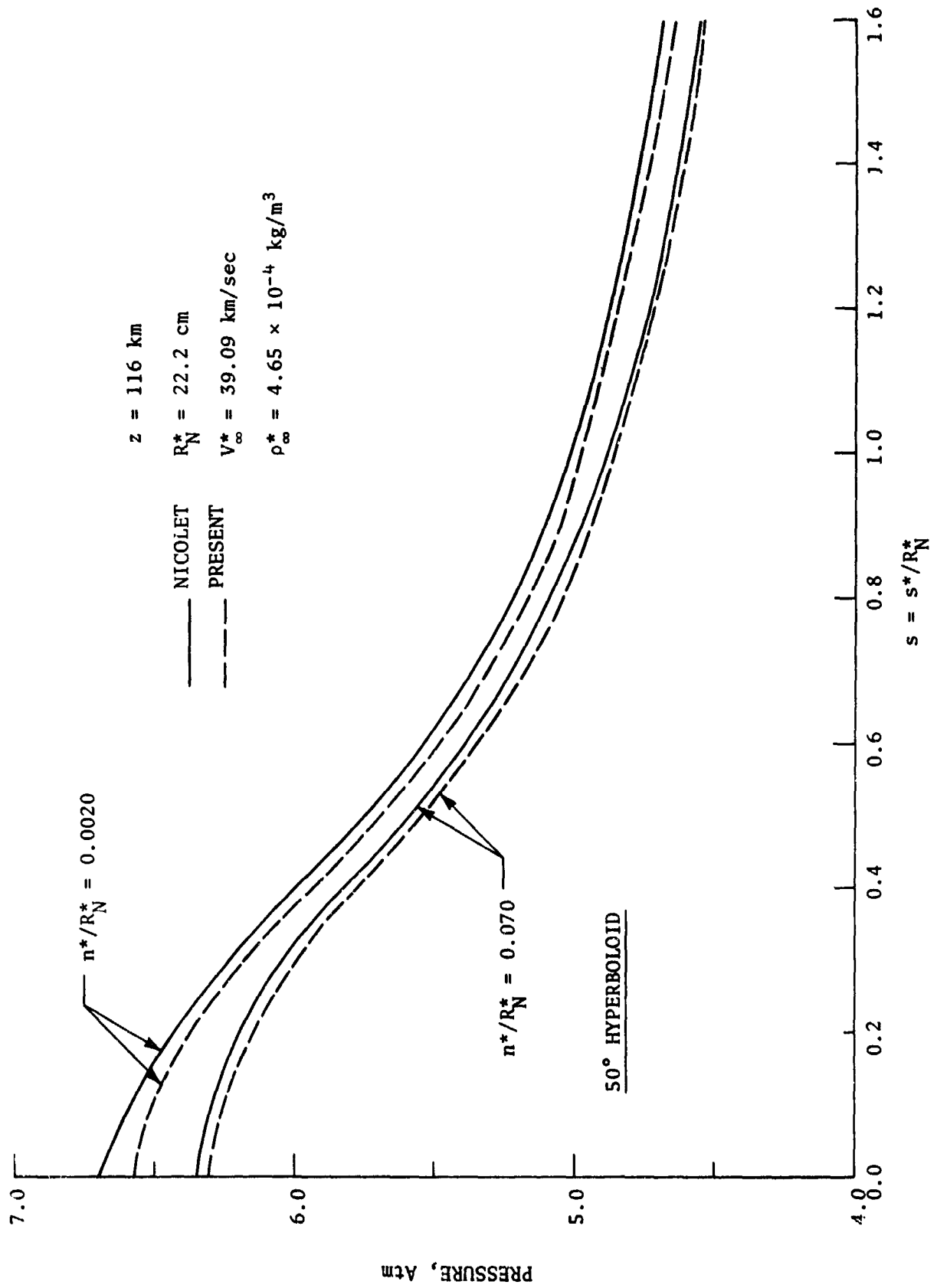
Figure 15. Pressure variation along the body coordinate at two different locations
(n = 0.002 and 0.07) in the shock layer (50° hyperboloid, z = 116 km).
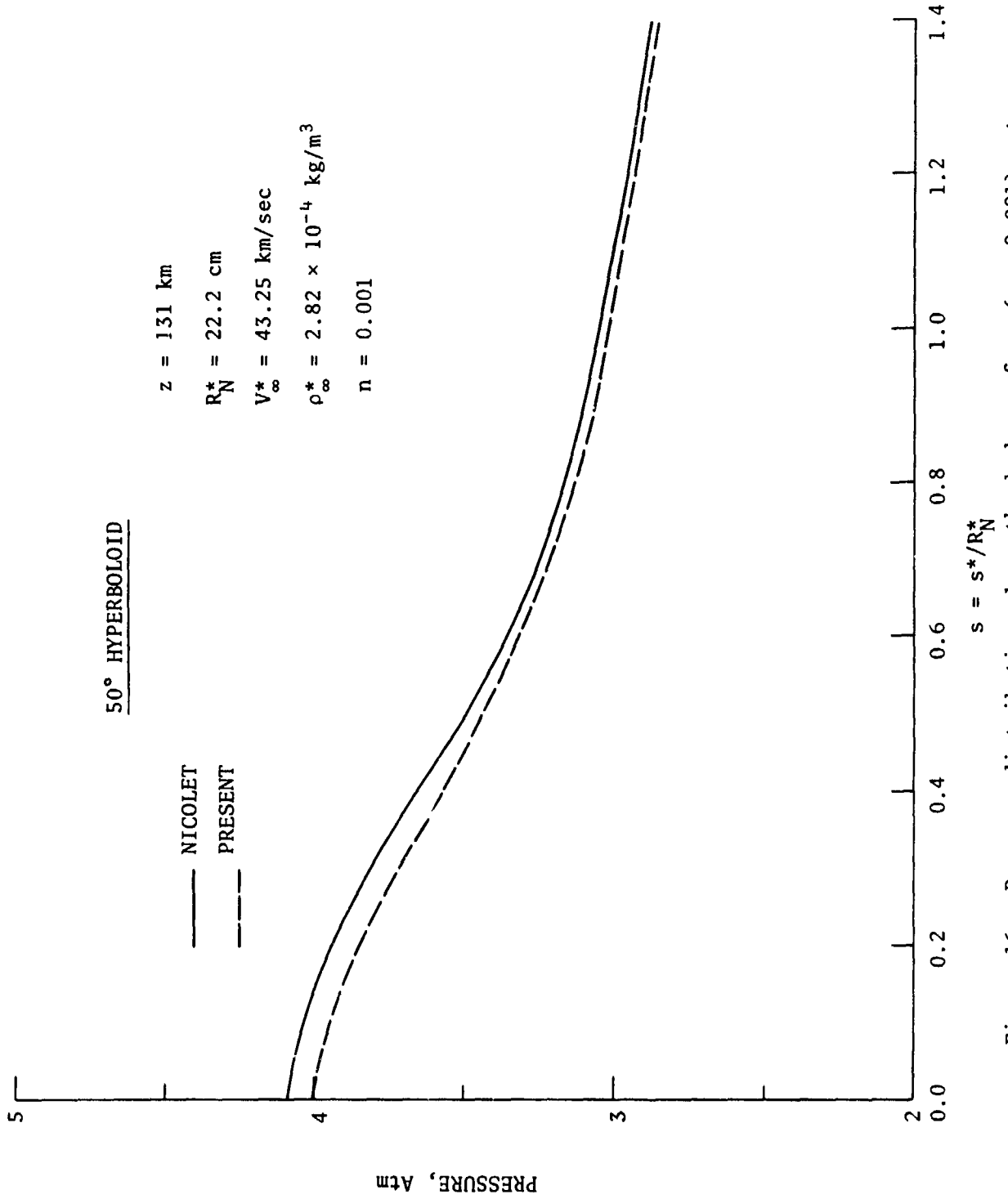
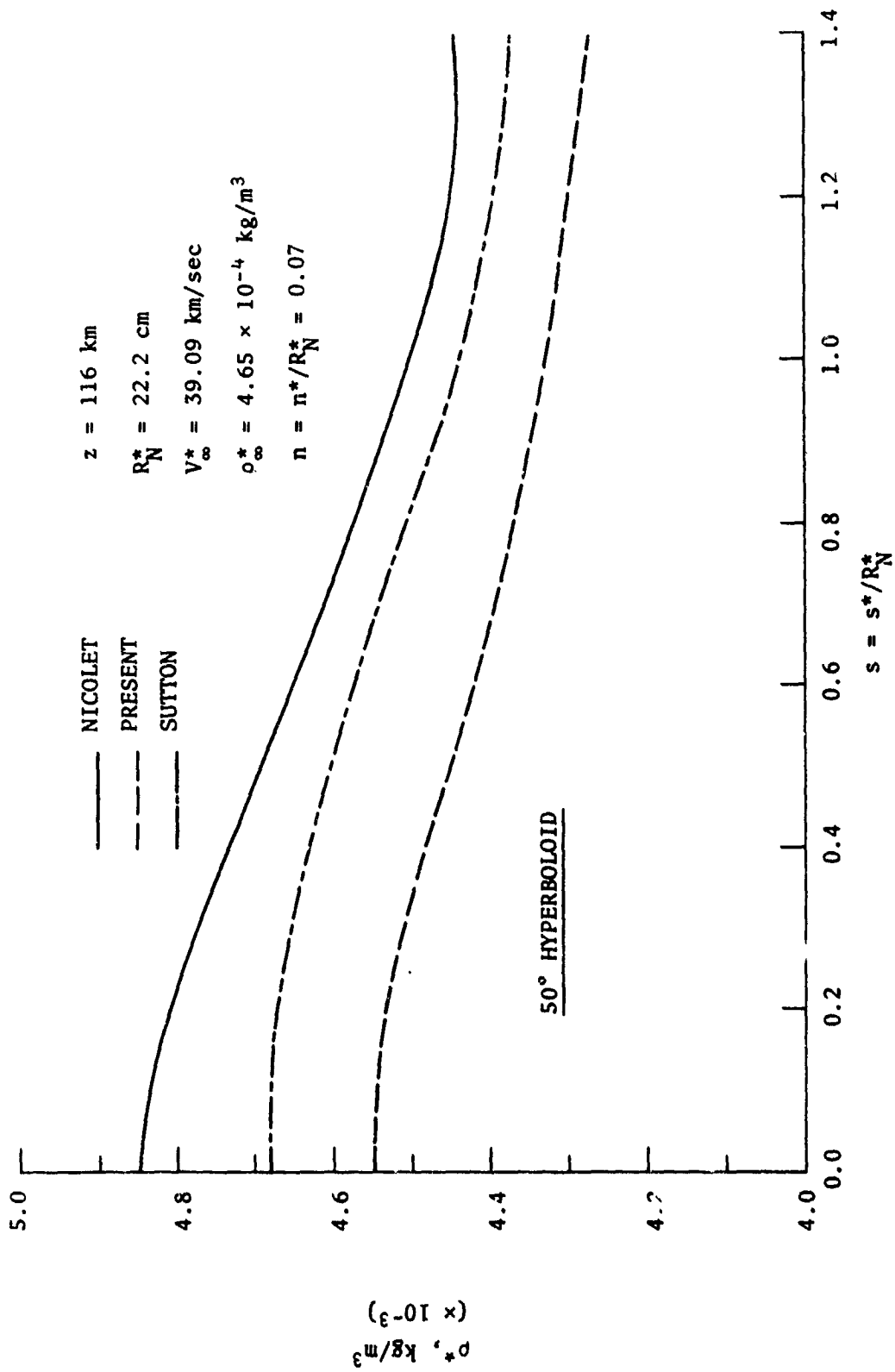Figure 16. Pressure distribution along the body surface (n = 0.001) entry conditions at z = 131 km (50° hyperboloid).

43

Figure 17. Density variation behind the shock (n = 0.07) with distance along the body surface (50° hyperboloid, z = 116 km).

44

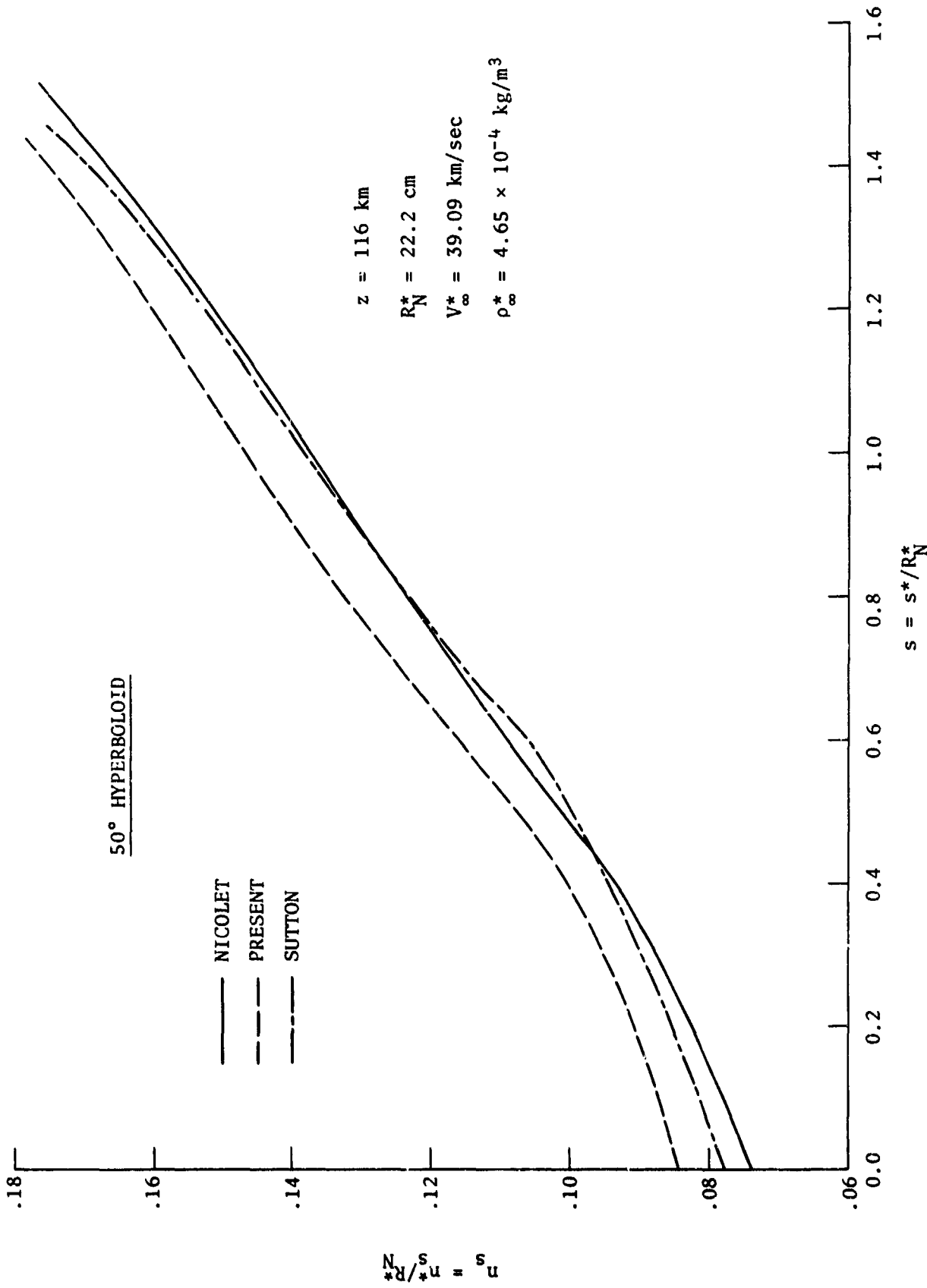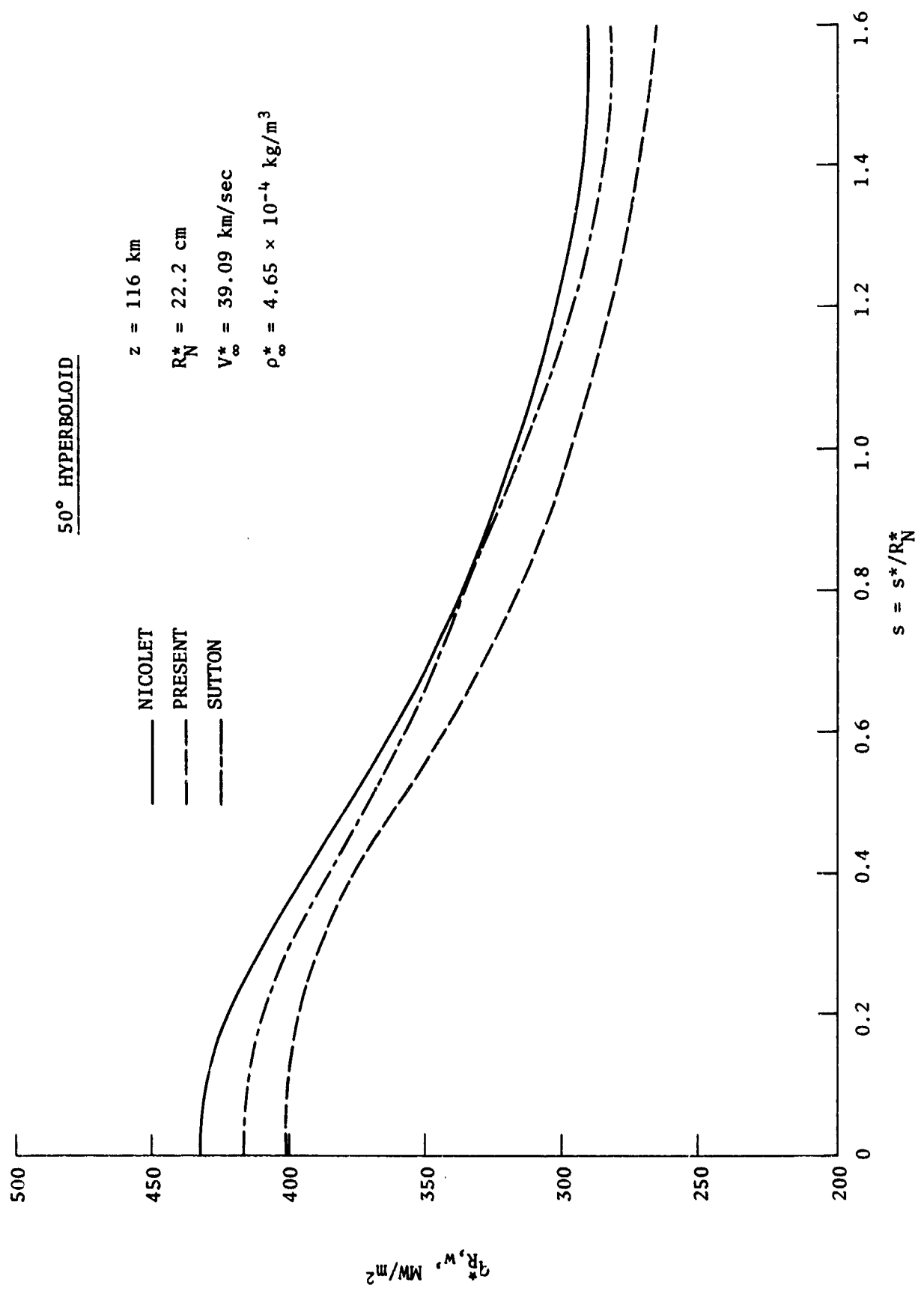Figure 18. Shock standoff variation with distance along the body surface (50° hyperboloid, z = 116 kn.).

Figure 19. Radiative heating along the body for entry conditions at z = 116 km (50° hyperboloid).

50° HYPERBOLOID

z = 116 km

$R_N^* = 22.2$ cm

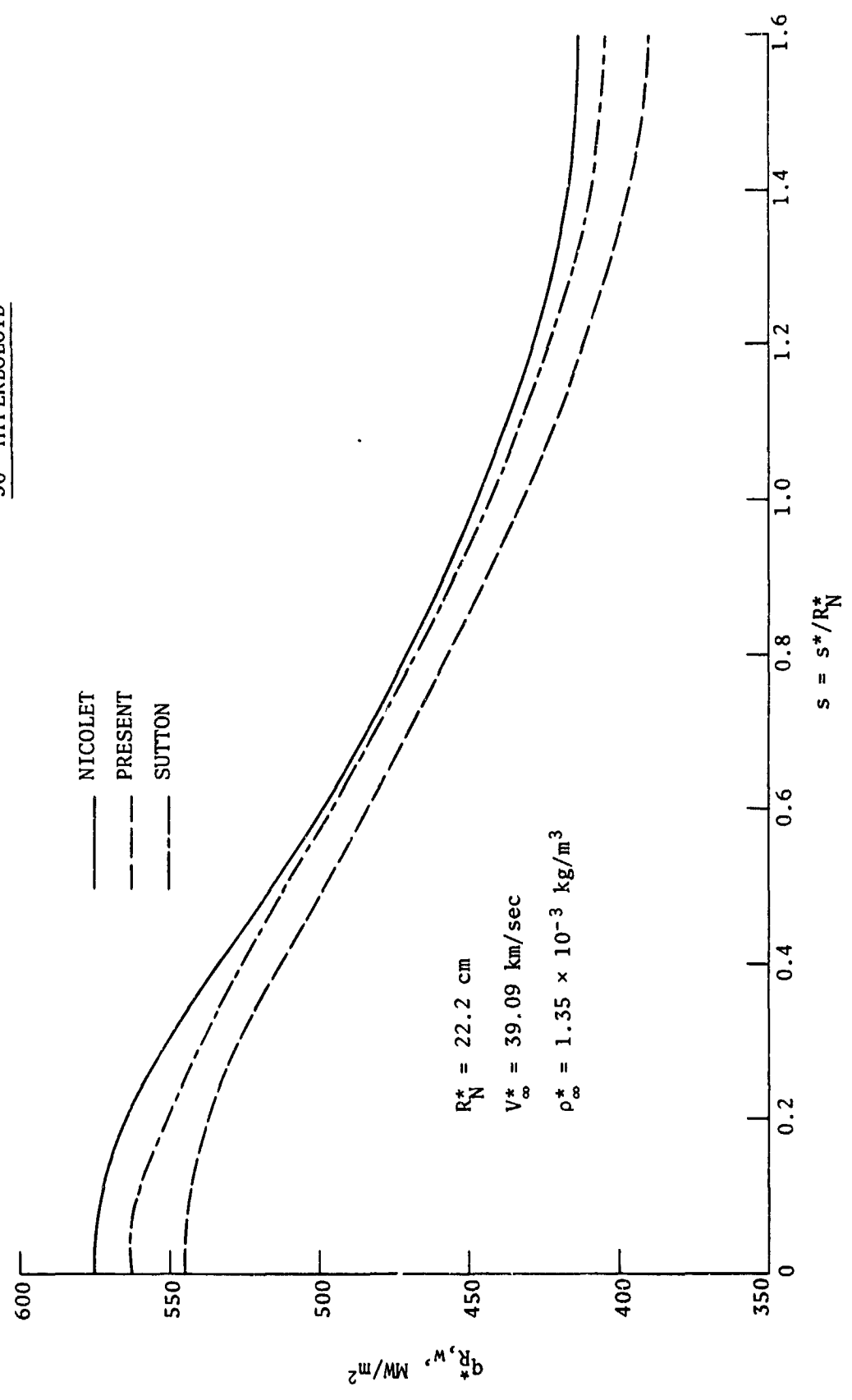$V_\infty^* = 39.09$ km/sec

$\rho_\infty^* = 4.65 \times 10^{-4}$ kg/m^3

NICOLET

PRESENT

SUTTON

$s = s^*/R_N^*$

$q_{R,w}^*$, MW/m^2

Figure 20. Radiative heating along the body for free-stream density higher than at z = 116 km (50° hyperboloid).

50° HYPERBOLOID

NICOLET
PRESENT
SUTTON

$R_N^* = 22.2$ cm

$V_\infty^* = 39.09$ km/sec

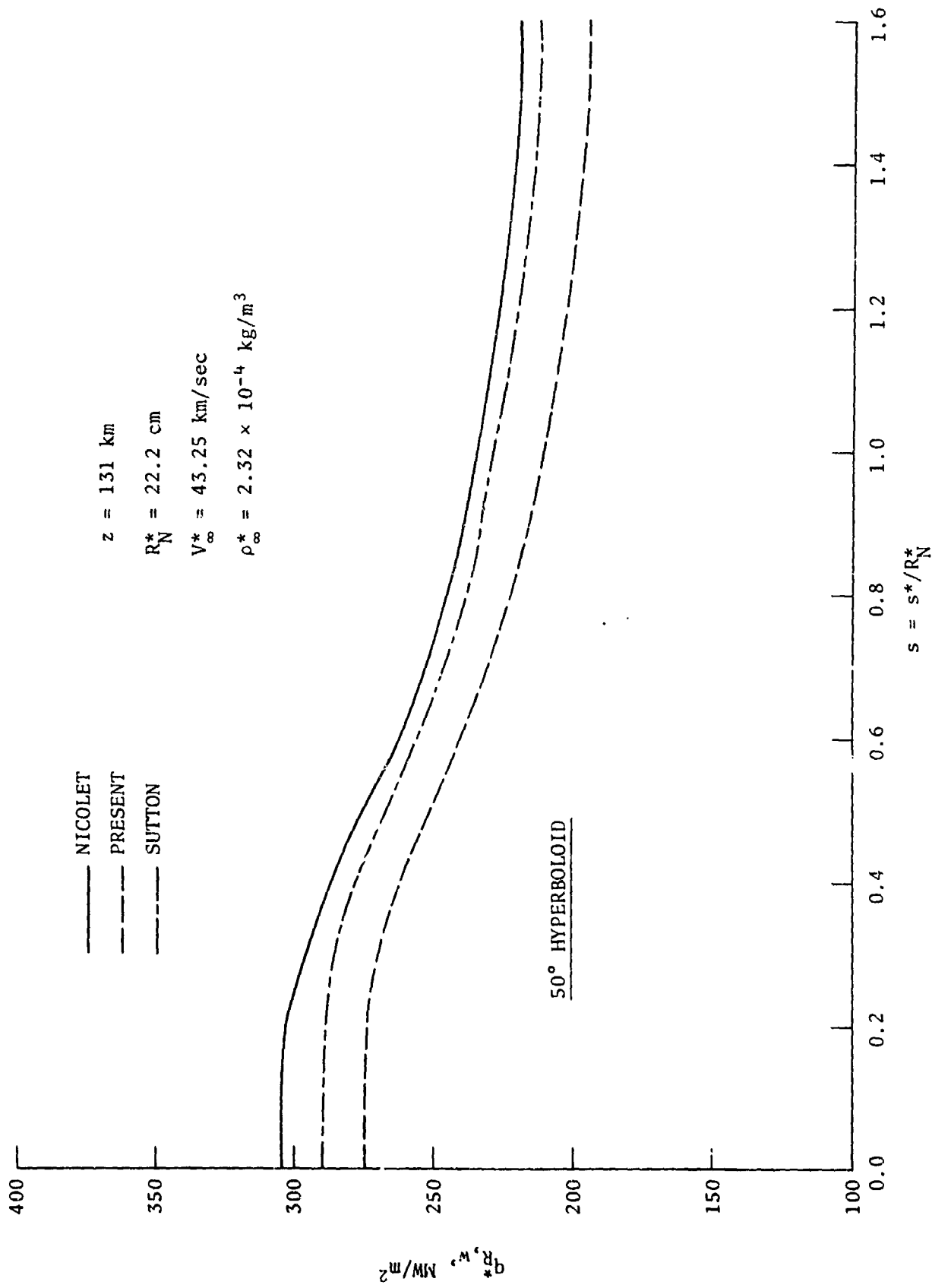$\rho_\infty^* = 1.35 \times 10^{-3}$ kg/m^3

$s = s^*/R_N^*$

$q_{R,w}^*$, MW/m^2

Figure 21. Radiative heating along the body for entry conditions at z = 131 km (50° hyperboloid).

48